Mineralization potential of water-dissolved CO 2 and H 2 S injected into basalts as function of temperature: Freshwater versus Seawater

Chiara Marieni, Martin Voigt, Deirdre E Clark, Sigurður R Gíslason, Eric H Oelkers

To cite this version:

Chiara Marieni, Martin Voigt, Deirdre E Clark, Sigurður R Gíslason, Eric H Oelkers. Mineralization potential of water-dissolved CO 2 and H 2 S injected into basalts as function of temperature: Freshwater versus Seawater. International Journal of Greenhouse Gas Control, 2021, 109, pp.103357. 10.1016/j.ijggc.2021.103357 . hal-03386376

HAL Id: hal-03386376
https://hal.science/hal-03386376

Submitted on 19 Oct 2021

Mineralization potential of water-dissolved CO_2 and H_2S injected into basalts as function of temperature: Freshwater versus Seawater

Author names and affiliations: Chiara Marieni [a,*], Martin Voigt [b], Deirdre E. Clark [c], Sigurður R. Gíslason [b], Eric H. Oelkers [a,b]

[a] Géosciences Environnement Toulouse (GET), CNRS UMR 5563, 14 Avenue Edouard Belin, Toulouse 31400, France

[b] Institute of Earth Sciences, University of Iceland, Sturlugötu 7, 102 Reykjavík, Iceland

[c] Iceland GeoSurvey (ÍSOR), Grensásvegur 9, 108 Reykjavík, Iceland* Corresponding author, chiara.marieni@get.omp.eu

Highlights

- Reaction path models quantified gas-charged waters/basalt interactions
- Gas-charged freshwater and seawater compared
- Geochemical reactions modelled at temperatures from 25 to 260 °C
- Optimal conditions for subsurface mineralization of CO_2 and H_2S identified

Abstract

Mineralization of freshwater-dissolved gases, such as CO_2 and H_2S, in subsurface mafic rocks is a successful permanent gas storage strategy. To apply this approach globally, the composition of locally available water must be considered. In this study, reaction path models were run to estimate the rate and extent of gas mineralization reactions during gas-charged freshwater and seawater injection into basalts at temperatures of 260, 170, 100, and 25 °C. The calculations were validated by comparison to field observations of gas-charged freshwater injections at the CarbFix2 site (Iceland). The results show that more than 80% of the injected CO_2 dissolved in freshwater or seawater mineralizes as Ca and Fe carbonates at temperatures ≤170 °C after reaction of 0.2 mol/kgw of basalt, whereas at 260 °C much lower carbon mineralization rates are observed in response to the same amount of basalt dissolution. This difference is due to the competition between carbonate versus non-carbonate secondary minerals such as epidote, prehnite, and anhydrite for Ca. In contrast, from 80 to 100% of the injected H_2S is predicted to be mineralized as pyrite in all fluid systems at all considered temperatures. Further calculations with fluids having higher CO_2 contents (equilibrated with 9 bar pCO_2) reveal that i) the pH of gas-charged seawater at temperatures ≤170 °C is buffered at ≤6 due to the precipitation of Mg-rich aluminosilicates, which delays CO_2 carbonation; and ii) the most efficient carbonation in seawater systems occurs at temperatures < 150 °C as anhydrite formation is likely significant at higher temperatures.

Keywords

Mineral storage / Carbon Dioxide (CO_2) / Hydrogen Sulfide (H_2S) / Reaction path modelling / Freshwater / Seawater

1. Introduction

The 2018 IPCC report concluded that all pathways that limit global warming to 1.5 °C above pre-industrial levels require some carbon capture and storage technology (Rogelj et al., 2018). Permanent storage by *in situ* mineral carbonation, a strategy enhancing a natural process, is one long-term carbon dioxide (CO_2) storage option (e.g., Metz et al., 2005; Oelkers et al., 2008; Pacala and Socolow, 2004; Power et al., 2013; Sanna et al., 2014). Mafic and ultramafic rocks provide the best candidates for such storage due to their relatively fast dissolution rates and their high content of divalent cations, such as Mg^{2+}, Ca^{2+} and Fe^{2+}, required for the carbonate mineral formation (Gislason and Oelkers, 2014; Kelemen and Matter, 2008; McGrail et al., 2016; Schaef et al., 2010). The effects of rock composition and crystallinity, extent of reactions, and water chemistry on secondary mineralogy have been explored by a number of past experimental studies focused on freshwater-basalt-CO_2 interactions (Galeczka et al., 2014; Gislason and Oelkers, 2003; Gudbrandsson et al., 2011; Gysi and Stefánsson, 2012a, b; Luhmann et al., 2017; Marieni et al., 2018; Oelkers and Gislason, 2001; Peuble et al., 2015; Schaef and McGrail, 2009; Schaef et al., 2009; Sissmann et al., 2014; Wolff-Boenisch et al., 2004a, 2006; Wolff-Boenisch et al., 2004b). Reaction path simulations have provided insight into these basalt alteration processes and the effects of high CO_2 partial pressures (pCO_2) on dissolution and precipitation reactions (Gysi and Stefánsson, 2008; Rosenbauer et al., 2012). Field observations of alteration products and the related changes in aqueous solutions at sites where CO_2 is injected into the subsurface have advanced our understanding of the timescales of such fluid-rock interactions. For example, the CarbFix process, where gases are dissolved into water before or during their injection into subsurface reactive basalts, has been demonstrated to be a safe and cost-effective approach to limiting CO_2 and hydrogen sulfide (H_2S) emissions as the gases are mineralized within two years (Gunnarsson et al., 2018; Matter et al., 2016; Snæbjörnsdóttir et al., 2018a). Large volumes of water, however, are required to dissolve the gases using this method; approximately 32 tons of freshwater are needed to dissolve each ton of CO_2 at 25 °C and 25 bar pCO_2 (Snæbjörnsdóttir et al., 2020). This requirement limits the CarbFix approach geographically to where ample freshwater resources are located near suitable reactive rock formations. On the other hand, porous basalts near the continental margins have huge potential storage capacities adjacent to nearly unlimited supplies of seawater (Goldberg et al., 2008; Marieni et al., 2013; Snæbjörnsdóttir and Gislason, 2016). This observation suggests that the CarbFix approach could be applied to these regions by the injection of gas-charged seawater into submarine basalts. Yet, the use of seawater instead of freshwater for this purpose is not straightforward because the high amount of salts and sulfates present in seawater can dramatically alter the reaction paths and rates of both gas capture from point sources and the mineralization of CO_2 injected into the subsurface (e.g., Rosenbauer et al., 2012; Xu et al., 2007). For example, injection of seawater during industrial processes often leads to pipe clogging (e.g., Bader, 2007; Dai et al., 2017), and reactions between seawater and basalts can lead to the formation of permeability-destroying clay minerals in submarine basalt formations (e.g., Wolff-Boenisch and Galeczka, 2018; Wolff-Boenisch et al., 2011).

This study was designed to assess the potential of extending the CarbFix approach for the capture and subsurface mineral fixation of carbon and sulfur. Reaction path models were created to predict the rate and extent of subsurface geochemical reactions in basaltic reservoir rock in response to the injection of CO_2- and H_2S-charged freshwater and seawater as a function of temperature. These model calculations focus on i) identifying the main differences between the use of freshwater versus seawater for the injection of CO_2 and H_2S into subsurface basalts for mineral carbonation, ii) investigating the temperature limits of CO_2-charged injections, and iii) identifying the optimal temperature and fluid composition for the mineralization of CO_2 and H_2S gas mixtures within basaltic reservoirs.

2. Model calculations

2.1. Reaction path modelling

This study is largely based on thermodynamics via reaction path calculations. The reaction path models created in this study are used to predict the distribution of mineral reaction products occurring in response to the injection of gas-charged aqueous fluids while these fluids travel through a basaltic reservoir (**Figure 1**). Focus is made to determine the effect of varying temperature (from 25 to 260 °C) and fluid composition (freshwater or seawater) on the mineral-fluid interactions. Four distinct temperatures were chosen to give an overview of the effect of this parameter on carbonation potential. The modelled system was divided into ten sequential reaction steps to track fluid-rock interactions as a function of basalt dissolution. In each step, a fixed quantity of basalt was dissolved into the injected fluid and secondary minerals were allowed to precipitate until the system attained local thermodynamic equilibrium. The identity of secondary minerals allowed to form in the calculations was based on thermodynamic constraints and past field observations (see below). Precipitated minerals were not allowed to react in subsequent reaction steps, i.e. their precipitation was considered non-reversible. This was done to simulate fluids flowing in a reservoir, which constantly moves away from the minerals precipitated from this fluid.

All the calculations in this study were performed using the PHREEQC software package (v3) (Parkhurst and Appelo, 2013) together with the *carbfix.dat* (v1.1.0) thermodynamic database (Voigt et al., 2018a). Reaction path calculations were performed rather than the more detailed reactive transport calculations to generate site independent results, as well as to avoid uncertainties introduced by the estimation of mineral-fluid interfacial surface areas and the use of laboratory measured mineral dissolution and precipitation kinetics.

The reaction path model was parameterized and validated using the results from the ongoing CarbFix2 injection (Clark et al., 2018; 2020; Gunnarsson et al., 2018). In the CarbFix2 project, gas-charged water from the Hellisheiði geothermal power plant (SW Iceland) is injected into a hydrothermally altered basaltic reservoir with temperatures of ~260 °C (Clark et al., 2020; Gunnarsson et al., 2018; Snæbjörnsdóttir et al., 2018b). During the first phase of the CarbFix2 injection, up to July 2016, approximately 25% of the water-soluble gases from the power plant’s exhaust gas stream containing 63 vol% CO_2, 21 vol% H_2S, 14 vol% H_2, and 2 vol% of other gases such as Ar, CH_4, and N_2 were dissolved in a scrubbing tower into 20 °C condensed steam collected from the power plant’s turbines. The resulting gas-charged water was then transported to injection wells. Effluent water was co-injected into the wells with the gas-charged water, and these two water streams mixed in the well before entering the host rock. Three geothermal wells are used to monitor the geochemical evolution of fluids and assess the magnitude of gas mineralization. These wells are located 984 m (HE-31), 1356 m (HE-48), and 1482 m (HE-44) downstream from the dominant injection well (Clark et al., 2020; Gunnarsson et al., 2018). Mass balance calculations on sampled well fluids, taking account of non-reactive chemical tracers, were used to determine the fraction of the injected and formation water reaching each monitoring well, assuming non-reactive mixing. For field validation, a mixing final step was performed on the modelled fluid with formation waters (**Figure 1**). This accounts for fluid mixing within the reservoir near the monitoring wells as each monitoring well passes through three distinct hyaloclastite water feedzones (Snæbjörnsdóttir et al., 2018b). The mixing ratio used in the validation model calculation was chosen to be that of the fluids sampled from the monitoring well HE-31 on 3 November 2015, which contained 84 vol% formation water and 16% injected water based on tracer test results reported by Gunnarsson et al. (2018). Data from the other monitoring wells were not used for model validation because of the uncertainties on the various fluid flow paths (e.g., different injected water paths to each monitoring well and/or variable reactive paths depending on time).

The secondary mineralogy in the freshwater injection models was constrained by the mineralogy of alteration phases described in the literature for on-shore basalt formations (Alfredsson et al., 2013; Helgadóttir, 2011; Kristmannsdóttir, 1979; Larsson et al., 2002; Schiffman and Fridleifsson, 1991; Snæbjörnsdóttir et al., 2018b; Thien et al., 2015). The seawater injection models were validated using observations of alteration mineral zones described in the literature for the oceanic crust (Alt, 1995) and further field observations (e.g., Alt et al., 1996; Davis et al., 1997; Fisher et al., 2011).

Note that Daval (2018) speculated, based on some observations of Trias et al. (2017), that part of the carbon fixation during the original CarbFix injection could be due to biologic activity leading to the formation of subsurface organic material. The analysis of carbon isotopes at the original CarbFix injection site, where the injected carbon was mineralized at 35 °C, indicates, however, that bio-fixing was negligible. Moreover, it is highly unlikely that biologic activity influenced to any extent the carbon fixation during the ongoing CarbFix2 injections, as carbon fixation in this system is occurring at temperatures in excess of 250 °C. As such, the potential carbon fixation by subsurface biota has not been considered in this study.

2.2. Thermodynamic dataset and reactant compositions

All reaction path calculations reported in this study were performed using the *carbfix.dat* thermodynamic database (Voigt et al., 2018a). The *carbfix.dat* database is based on the *core10.dat* database (Neveu et al., 2017), which itself is largely derived from the widely used *llnl.dat* database compiled at the Lawrence Livermore National Laboratory. The *carbfix.dat* database corrects several errors, only contains thermodynamics data for reactions for which equilibrium constants, K, were available (as opposed to constants estimated based on the assumption of constant reaction enthalpy change, $\Delta_r H$), and only contains phases and species for which molar volumes are available, allowing the PHREEQC computer code to estimate the pressure dependence of equilibrium constants. The molar volumes listed in this database were also used to calculate the volume of the secondary minerals as a function of reaction progress.

The bulk chemical composition of Stapafell basaltic glass (Gysi and Stefánsson, 2011; Oelkers and Gislason, 2001) normalised to one mol of Si, was used as the only phase initially present in the rock formation; the composition of such glass is provided in **Table 1**. This basaltic glass composition is in agreement with normalized field data and was used in all the reaction path models to allow direct comparison of computed results. The freshwater composition used in some of the calculations was set to that of the pre-injection effluent water collected near the Hellisheiði power plant as reported by Gunnarsson et al. (2018), whereas the seawater composition used in the other calculations was taken from Millero et al. (2008). The compositions of these waters are provided in **Table 2** together with the average composition of the formation waters sampled from monitoring well HE-31 before the gas-charged water injections (Clark et al., 2020), which was used in the final mixing step of the modelling to match model results to the observed monitoring well water composition.

In all the reaction path calculations, the power plant exhaust gases were first dissolved in pure water, consistent with the composition of condensed steam. This gas-charged water was subsequently mixed with either freshwater or seawater in the molar ratio of 0.3 parts gas-charged water to 0.7 parts either fresh or seawater; this ratio is based on the mixing ratio of the fluids injected during the CarbFix2 project (Clark et al., 2018). The resulting diluted gas-charged water contains either 30.8 or 32.0 mmol/kgw of dissolved inorganic carbon (DIC) and 22.4 or 42.4 mmol/kgw of dissolved sulfur (DS), for freshwater or seawater dilution, respectively (**Table 3**). These DIC values correspond to a fluid equilibrated with 1 bar of pCO_2. In the case of freshwater, almost all the carbon and sulfur in the injected mixture originates from the dissolved gas; in the case of seawater, almost all the carbon but only 21.9 mmol/kgw of sulfur (~52% of the total injected DS) are derived from the dissolved gas, with the remaining originating from the natural sulfate content of seawater. The choice to first dissolve the gases in pure water prior to their dilution in freshwater or seawater was made to enable clear comparisons among the model results.

The use of model input parameters replicating those from the CarbFix2 gas-charged water injection allows the validation of model results with field observations. In addition, the injection of more concentrated CO_2 fluids was also explored. For these latter calculations, identical fluids were used as in the original calculations other than they contained a higher CO_2 concentration. This higher concentration was taken equal to that of freshwater or seawater equilibrated with 9 bar CO_2 (**Table 3**), which is the injection pressure at the CarbFix2 injection well head (Clark et al., 2020). This results in injected dissolved CO_2 concentrations of ~127 and ~116 mmol/kgw, respectively, for the freshwater and seawater injections. In all calculations, carbon dioxide solubility was determined with the Peng-

Robinson equation of state (Peng and Robinson, 1976) as implemented in PHREEQC (Appelo et al., 2014).

The compositions, chemical formulas, molar volumes and thermal stability fields of the secondary phases considered in the reaction path calculations are listed in **Table 4**. The thermal stability field defines the temperature range in which a mineral has been observed in experimental and/or field studies. Consistent with field observations, dolomite was not allowed to precipitate, and the formation of reduced aqueous carbon species, C^{-4} or methane (CH_4), was restricted. The volume of the dissolving basaltic glass was calculated using a molar weight of 123 g/mol and density of 2.851 g/cm^3 (Galeczka et al., 2014). The rock volume changes reported below are defined as the difference between the volume of the dissolved rock and the total volume of the precipitated secondary minerals. As such, these do not correspond to rock porosity changes. Rock porosity changes would depend on the amount of basalt dissolved and secondary minerals formed at each point in the system, which will be a function of fluid rates, rock-fluid interfacial surface area, and mineral reaction rates. Such factors are not explicitly considered in this study. Also, the effect of the presence of dissolved gas in the fluid phase on reservoir rock volume changes was determined by comparing each gas-charged reaction path calculation to a corresponding reaction path calculation result with either gas-free freshwater or seawater (**Table 2**).

3. RESULTS

3.1. Reaction path field validation

The results from the reaction path calculations, performed for the injection of freshwater-dissolved CO_2 into basalts at 260 °C and thereby mimicking the CarbFix2 injection are shown in **Figure 2** along with the corresponding field observations reported by Clark et al. (2020). Ten steps of 0.02 mol basalt dissolution per kg H_2O were required prior to the non-reactive mixing of the resulting fluid with the background water to obtain the fluid composition measured at monitoring well HE-31. A total of 0.2 mol basalt dissolution was chosen for this calculation to match the results of Clark et al. (2020). This 0.2 mol/kgw basaltic glass corresponds to a mass of 25 g or a volume of 8.6 cm^3 of basalt dissolved per kg water.

The calculated final pH of 7.36 obtained in this calculation after fluid-rock interaction is in close agreement with the measured field *in situ* pH of 7.31 (**Figure 2a**). A close match is also found between calculated and measured DIC and DS (**Figure 2b**); the calculated final fluid values were 9.93 and 1.86 mmol/kgw, whereas the corresponding field measured values were 10.58 and 2.14 mmol/kgw, for DIC and DS, respectively. Similarly, the calculated major element fluid concentrations match well with the corresponding field values, with no significant systematic differences (**Figure 2c**). Note, however, an underestimate of ~20% in the Si concentrations and a ~15% overestimate of the Na values were obtained in the calculation. The model results indicate the formation of calcite, albite, prehnite, Mg-chlorite (clinochlore) and epidote (**Figure 2d**), which is in agreement with the geochemical calculations based on monitoring data as well as the geological description of the CarbFix2 site (Snæbjörnsdóttir et al., 2018b). The model-field comparison of the saturation indices of all the secondary minerals listed in **Table 4** for temperature conditions of 260 °C shows that most are in close agreement other than for those of Fe-bearing phases, which are underestimated by the model calculations.

3.2. Reaction path calculations for gas-charged waters at 260 °C

A comparison of the results from the gas-charged freshwater and the gas-charged seawater reaction path model calculations at 260 °C are shown in **Figure 3**. In the freshwater system, the pH increases from 5.8 to 7.7, whereas in the seawater system the pH follows a different trend, decreasing from 5.5 to 4.1 in response to the dissolution of the first 0.02 mol of basaltic glass, and then slowly rising back to ~5.4 after the dissolution of 0.14 additional moles of basaltic glass.

The DIC and DS mineralized are shown as a percentage of the amount of these gases originally injected in **Figure 3 c and d**. A substantial amount of the originally injected sulfur is mineralized in response to 0.2 mol basalt dissolution per kg of injected solution, with freshwater mineralizing around 80% (~17.4 mmol/kgw), and seawater almost 100% (~41.9 mmol/kgw, of which 22.4 mmol/kgw originates from the gas-charged solution) of the injected dissolved sulfur. In contrast, the efficiency of DIC mineralization is substantially different if injected via freshwater compared to seawater after the dissolution of 0.2 mol of basalt. Gas-charged freshwater-basalt interaction is estimated to mineralize ~40% of the originally injected DIC (~11.6 mmol/kgw), whereas gas-charged seawater-basalt interaction removes only ~10% (~3.2 mmol/kgw) of the originally injected DIC. This lower CO_2 uptake by the solids in the latter case is the result of the stability and formation of non-carbonate Ca-bearing minerals (see below).

In both the freshwater and the seawater systems, the CO_2 is mineralized as calcite, whereas dissolved sulfur precipitates only as pyrite in freshwater, and as pyrite and anhydrite in seawater. The other minerals observed as secondary phases during the dissolution-precipitation reaction path in freshwater, in descending order of molar abundance, are quartz, epidote, Mg-chlorite (clinochlore), albite, prehnite, ilmenite, magnetite, and K-feldspar. In the seawater reaction path model, the secondary minerals are quartz, Mg-chlorite, albite, epidote, hematite, ilmenite, and magnetite. Prehnite and K-feldspar are observed only during the freshwater injection and hematite only during the seawater injection. Furthermore, quartz, epidote, and magnetite are more abundant during the freshwater injection, clinochlore and albite more abundant during the seawater injection, while ilmenite shows similar abundances from either injection. In these 260 °C calculations, chlorites were allowed to precipitate rather than smectites consistent with the observations by Alt (1995) and Snæbjörnsdóttir et al. (2018c) for seawater and freshwater injections, respectively.

The efficiency of CO_2 mineralization can be visualized by assessing the distribution of Ca among the various secondary phases (**Figure 3 g and h**). In the freshwater system, Ca is taken up, in descending order of abundance, by epidote, prehnite, and calcite, with prehnite being predominant compared to the other phases during the initial reaction path steps. In the seawater system, most of the Ca is taken up by anhydrite. It is only after the injected sulfate is consumed, after 0.12 mol of basaltic glass dissolution, that epidote and calcite begin to form, with epidote being predominant over calcite.

The combined dissolution-precipitation reactions predicted to occur leads to an increase in the rock volume per kg of injected solution in both systems: +1% for the freshwater case, and +11% for seawater. Moreover, the gas-charged seawater-basalt system shows a rock volume increase during the first reaction step, whereas the rock volume increase in the freshwater system begins only after the dissolution of 0.10 mol of basaltic glass. This volume increase is largely the result of the formation of hydrated minerals, such as chlorites, where the water included in the structure increases the mineral volume.

3.3. Reaction path calculations for gas-charged waters at 170 °C

The results from both the gas-charged freshwater and the gas-charged seawater reaction path calculations at 170 °C are illustrated in **Figure 4**. In the freshwater system, the aqueous solution pH increases almost linearly from 5.0 to 9.7 with increasing basaltic glass dissolution, whereas in the seawater system the pH first sharply increases from 4.8 to 5.6 in response to the dissolution of the first 0.02 mol of basaltic glass, followed by a slow rise to 6.0.

At this temperature, both the freshwater and seawater injections indicate a similarly high percentage of injected sulfur mineralization, with the freshwater mineralizing around 96% (~21.5 mmol/kgw) of the initial DS, and the seawater mineralizing almost 95% (~40.2 mmol/kgw, of which 22.4 mmol/kgw originated from the dissolved gas) of the initial DS. Similarly, the mole percent of initial DIC sequestered is above 90% during both the freshwater and seawater system (~99% and ~92%, respectively). In the case of the freshwater injection, most of the DIC is mineralized before the first 0.12 mol of basaltic glass is dissolved, whereas about twice as much basalt dissolution (0.2 mol) is required to reach a similar DIC mineralization value in the seawater system.

As in the 260 °C reaction path calculations, the CO_2 is mineralized as calcite, whereas the DS precipitates as pyrite during the freshwater injection, but as both pyrite and anhydrite during the seawater injection. The other secondary phases calculated to form during the reaction path calculations in the freshwater systems, in descending order of abundance, are Mg-smectites, Ca-zeolites (laumontite and mordenite), ilmenite, Na-zeolite (analcime), Fe-smectites, K-smectites, magnetite, and K-feldspar. In the seawater system, the secondary minerals are Mg-smectites, hematite, ilmenite, and Fe-smectite. Zeolites, magnetite, K-smectites and K-feldspar are observed only during freshwater injection, whereas hematite only during seawater injection. Fe-smectites are more abundant during the freshwater injection, whereas Mg-smectites are more abundant during the seawater injection.

At this temperature in the freshwater system, Ca is taken up, in descending order of abundance, by calcite, mordenite and laumontite, with more than 60% of Ca being incorporated into calcite throughout the whole reaction path. During the seawater injection, calcite and anhydrite compete for Ca, with anhydrite taking up to ~75% of the available Ca in the initial reaction step, and ~35% after 0.06 mol of basaltic glass has dissolved. The results of these calculations suggest a similar increase in rock volume in both modelled gas-charged water injections as a function of basalt dissolution: +18% for the freshwater system, and +14% for the seawater system. This volume increase is mostly due to the formation of clay minerals and zeolites, which are hydrated minerals.

3.4. Reaction path calculations for gas-charged waters at 100 °C

The results from both the gas-charged freshwater and the gas-charged seawater reaction path calculations at 100 °C are shown in **Figure 5**. In the freshwater system, the pH increases almost linearly from 4.7 to 10.4, whereas in the seawater system, the pH first increases sharply from 4.6 to 5.8 in response to the dissolution of the first 0.02 mol of basaltic glass, and then increases more slowly to 6.9.

Both injected fluids show comparable high percentages of the injected carbon mineralization, with gas-charged freshwater-basalt interaction mineralizing almost 100% (~30.8 mmol/kgw) of the initial DIC and gas-charged seawater-basalt interaction mineralizing almost 99% (~31.6 mmol/kgw) of the initial DIC. The DS is nearly completely mineralized during the injection of gas-charged freshwater, but only ~74% of this sulfur is mineralized during the injection of gas-charged seawater; yet, almost 100% of the injected H_2S is mineralized even during seawater injection. The sulfur remaining in the fluid phase is in the form of sulfate. For both the gas-charged freshwater and seawater injections, most of the DIC is mineralized before 0.14 mol of basaltic glass has dissolved, whereas only half of this basalt is required to mineralize most of the H_2S.

At this temperature, in both the freshwater and seawater systems, the CO_2 is mineralized mainly as calcite, with lesser amounts of ankerite precipitating near the end of the calculations. The DS is mineralized as pyrite during both the freshwater and seawater injections, with only a minor amount of anhydrite formed due to gas-charged seawater injection at this temperature. The other minerals observed as secondary phases throughout the dissolution-precipitation reaction path during freshwater injections, in descending order of molar abundance, are Mg-smectites, Ca-zeolites (mordenite and thomsonite), ilmenite, Fe-smectites, K-smectites, and celadonite. In the seawater system, the secondary minerals are Mg-smectites, hematite, ilmenite, and Ca-zeolites (mordenite and thomsonite). Fe-smectites, K-smectites and celadonite are observed only in the freshwater system, whereas hematite was only observed to form in the seawater system. Ca-zeolites are more abundant during the freshwater injection, whereas Mg-smectites are more abundant during the seawater injection.

In the freshwater system, calcium is consumed in descending order of molar abundance by calcite, ankerite, mordenite and laumontite, with ~57% of Ca incorporated into calcite throughout the whole path, ~3% by ankerite, and ~40% by zeolites. In the seawater system, the same minerals compete for Ca, with calcite consuming ~55% of the available Ca throughout the whole reaction, and about ~15% each is consumed by zeolites, ankerite, and anhydrite.

The volume of the precipitating phases is +18% larger than that of the dissolving basalt during the freshwater injection but only +14% during the seawater injection. This volume increase can be related to the abundance of both the smectitic clay minerals and the zeolites.

3.5. Reaction path calculations for gas-charged waters at 25 °C

The results from both the gas-charged freshwater and the gas-charged seawater reaction path models at 25 °C are illustrated in **Figure 6**. In the freshwater system, the pH increases almost linearly from 4.9 to 11.9 with increasing basaltic glass dissolution, whereas in the seawater system the pH increases linearly from 4.7 to 8.3 as 0.14 mol basalt is dissolved per kg of injected solution, but from this point on the pH remains nearly constant.

Both the freshwater and seawater injections mineralize more than 90% (~28.4 and 32.0 mmol/kgw, respectively) of the injected DIC. In contrast, the DS is almost completely mineralized during the freshwater injection, but only ~62% during the seawater injection (~26.4 mmol/kgw total, of which 22.4 mmol/kgw comes from the dissolved gas). Most of the DIC is mineralized in response to the first 0.12 mol of basaltic glass dissolution, whereas only half of this basalt dissolution is required to mineralize most of the DS. The sulfur remaining in the aqueous solution at the end of the calculation is mainly in the form of sulfate.

The injected CO_2 is primarily mineralized as calcite, while some ankerite is predicted to form in the seawater system. The DS precipitates as pyrite during both the freshwater and seawater injections. The other minerals observed as secondary phases during the dissolution-precipitation reaction path in freshwater, in descending order of molar abundance, are Mg-smectites, Ca-zeolites (chabazite and thomsonite), ilmenite, Fe-smectite, Na-smectite, K-smectite, and celadonite. In the seawater system, the secondary minerals are Mg-smectites, celadonite, hematite, ilmenite, K-smectite, Ca-zeolite (thomsonite), and Na-smectite. Fe-smectites are formed only in response to the injection of gas-charged freshwater, whereas hematite precipitates only in the response to the injection of gas-charged seawater. Ca-zeolites are more abundant during the injection of freshwater, with Mg-smectites and celadonite more abundant during the injection of seawater.

In the freshwater system, aqueous calcium is consumed, in order of abundance, calcite, chabazite and thomsonite, with ~70% of the Ca precipitating as calcite, and the rest as Ca-zeolites. During the seawater injection, calcite, ankerite and thomsonite compete for

Ca, with calcite consuming ~65% of the available Ca over the reaction path, but significant amounts of ankerite and zeolite are also calculated to form. As was the case for the higher temperature models, the formation of these minerals leads to a net volume increase in the solid phases in both freshwater and seawater systems of 9 and 12%, respectively.

3.6. Reaction path calculations for CO_2-rich waters

The results from the additional reaction path calculations run for systems having higher DIC concentrations are summarized in **Figure 7**. In these calculations, the freshwater or seawater was first equilibrated with 9 bar CO_2 at 67 °C prior to its injection. For these calculations, 1 kg of initial gas-charged freshwater or seawater was reacted in 70 consecutive reaction steps, each adding 0.02 mol of basaltic glass. This increased mass of basaltic glass dissolution was necessary to mineralize the CO_2 in the injected waters, which have substantially higher carbon concentrations than in the previous model calculations.

In the case of the injection of either CO_2-rich freshwater or CO_2-rich seawater at temperatures ≤170 °C, the dissolution of 0.4 mol of basaltic glass was sufficient to mineralize ~90% of the injected CO_2, whereas around 4 times more basaltic glass dissolution was required for this mineralization at 260 °C due to the formation of other Ca-bearing secondary minerals. The fluid pH of the injected waters after 90% of the injected DIC was mineralized differed between the freshwater and the seawater system. For the freshwater injection this pH ranged from between 8.8 and 9.8, depending on temperature. The pH of the injected CO_2-rich seawater was more strongly buffered; the pH of the fluid phase after ~90% of the DIC had mineralized ranged from 5.7 to 6.4 at temperatures ≤170 °C but was 8.1 at 260 °C. As further DIC mineralized, the calculations for both the freshwater and seawater systems suggest that the pH continues to increase to above 10, which is higher than the maximum pH around 9 typically observed for groundwater isolated from the atmosphere in contact with alumino-silicate minerals (Langmuir, 1997). These anomalous high pH are due to the continued calculated precipitation of zeolites and clay at alkaline conditions. For example, thomsonite (**Equation 1**) and saponite-Fe-Mg (**Equation 2**) are predicted to form at pH 10 according to

$$5Al(OH)_4^- + 2Ca^{2+} + 4HSiO_3^- + NaHSiO_3 \rightarrow Ca_2NaAl_5Si_5O_{20}{:}6H_2O + 4H_2O + 5OH^- \qquad (1)$$

and

$$0.175Mg^{2+} + 0.35Al(OH)_4^- + 3Fe(OH)_3^- + 3.65HSiO_3^- \rightarrow Mg_{0.175}Fe_3Al_{0.35}Si_{3.65}O_{10}(OH)_2 + 2.7H_2O + 6.65OH^- \qquad (2)$$

The continued precipitation of these minerals at elevated pH in the calculations suggests some inconsistencies in the thermodynamic database for one or more of these phases or the aqueous species of their constituent metals at high pH.

The solid phases predicted to form according to the reaction path calculations were compared to the results of corresponding experimental data reported in a number of studies of high *p*CO_2 gas-charged water-basalt interaction (e.g., Gysi and Stefánsson, 2012a; Gysi and Stefánsson, 2012b; Kanakiya et al., 2017; Schaef et al., 2010; Shibuya et al., 2013; Sissmann et al., 2014), and to observations of mineral assemblages in CO_2-rich natural systems (Freedman et al., 2009; Nakamura and Kato, 2004; Neuhoff et al., 1999; Rogers et al., 2006; Schiffman and Fridleifsson, 1991; Shibuya et al., 2012). Similar to these past studies, our calculations exhibit the precipitation of carbonates and other non-carbonate phases such as chlorites, zeolites and clay minerals as the fluid pH increases (see **Appendix A**). Some differences are nevertheless evident. In contrast to the previous studies, amorphous silica was not predicted to precipitate during the 100 °C CO_2-rich freshwater reaction path calculations, despite it having been observed upon CO_2 input to the experimental systems at 75 and 150 °C by Gysi and Stefánsson (2012c), at 150 °C by Sissmann et al. (2014), and in West Greenland basalts altered at 80-125 °C by Rogers et al. (2006). Epidote was predicted to form in the model calculations during both the freshwater and seawater injections at 260 °C, similar to its presence as a secondary mineral reported in field studies of hydrothermally altered mafic systems (e.g., Freedman et al., 2009; Schiffman and Fridleifsson, 1991). Yet, this mineral was not detected at comparable temperatures during water-dissolved CO_2-basalt experimental studies (e.g., Gysi and Stefánsson, 2012b; Shibuya et al., 2013) or other field observations (e.g., Nakamura and Kato, 2004).

3.7. Reaction path model results for gas-free waters

Reaction path calculations with gas-free freshwater or seawater were included to better constrain the effect of the presence of injected gases on the rock volume changes. For the reaction path run in the presence of seawater at 170 °C, kaolinite was allowed to precipitate in addition to the already listed secondary minerals in the gas-charged system as it was computed to be supersaturated at times in the fluids phase. For the purpose of this study, only the output results on the rock volume changes were discussed below; yet all the reaction path calculation outputs were summarized and made available in **Appendix B**.

4. DISCUSSION

4.1. Gas-charged water injection: comparison with field data

The results of the reaction path calculations based on the CarbFix2 gas injection conditions (**Figure 2**) are in close agreement with the chemical composition of the fluid sampled from the field monitoring well HE31 during this injection (Clark et al., 2020). The modelled pH of this 260 °C freshwater injection matches the pH of the CarbFix2 monitoring fluids after the dissolution of about 0.2 mol of basalt. Also, the computed saturation states determined from the calculations agree well with the monitoring results for most minerals although they underestimate those of the Fe-bearing phases such as ankerite, pyrite, daphnite, and epidote. This underestimation is most likely related to the assumption of full oxidation-reduction (redox) equilibrium in the model calculations, while measured sulfide/sulfate redox couple concentrations were used to interpret the field-obtained monitoring data. These differences suggest that full redox equilibrium might not have been achieved in the CarbFix2 system in the field.

The mineral assemblages predicted to form by the reaction path calculations shown in **Figure 3** are similar to the observed secondary mineralogy produced by the freshwater hydrothermal alteration of basaltic rocks in natural analogues (e.g., Kristmannsdóttir, 1979; Snæbjörnsdóttir et al., 2018b), and gas-water-basalt interaction experiments performed at 250 °C (Stefánsson et al., 2011; Thien et al., 2015). Calculations indicate Mg-chlorite (clinochlore) precipitation throughout the whole reaction path, while epidote is calculated to precipitate only at pH >7, consistent with the mineralogy seen on the top of the chlorite-epidote zone of basalt alteration in the Hellisheiði reservoir (Snæbjörnsdóttir et al., 2018b). Albite formation reflects the process of albitization associated with the alteration of Ca-rich plagioclase as expected to occur at this temperature (Franzson et al., 2008; Snæbjörnsdóttir et al., 2018b). Model results also confirm field observations that DS mineralizes as pyrite earlier, in terms of the amount of basaltic glass dissolved, compared to the carbonation of DIC as calcite. Pyrite forms during the first reaction path steps up until the pH reached ~7, when its precipitation is slowed by epidote formation (Stefánsson et al., 2011). Significant amounts of calcite are calculated to begin forming at pH >7.3, consistent with the observations reported by Clark et al. (2020) where calcite only precipitated when sufficient basaltic glass has dissolved to neutralize the acidic injection fluids. At lower pH, the Ca-bearing mineral prehnite is predicted to precipitate. Another Ca-bearing phase potentially competing with calcite for aqueous calcium is tremolite (the Ca-Mg end-member of actinolite), which was found to be supersaturated in both the modelled and monitored fluids (**Figure 2**). Note, however, that actinolite is found in Icelandic geothermal systems only when temperatures exceed 280 °C (Kristmannsdóttir, 1979), so that its precipitation during the reaction path calculations was not allowed.

The results of DIC mineralization in the gas-charged seawater calculations can be compared with field studies of oceanic crust alteration (Alt and Teagle, 1999; Coggon et al., 2004; Coogan and Gillis, 2013; Gillis and Coogan, 2011; Rausch et al., 2013; Staudigel et al., 1989). On average, the carbonate content as $CaCO_3$ within the upper 600–700 m of global oceanic crust, equal to 10% of the average thickness of this crust, is ~1.5 wt% (Rausch, 2012). Though, within the uppermost 300 m of submarine volcanic basalts the carbonate abundance can reach as much as ~11 wt%, mainly as calcite, with carbonate veins commonly filled at temperatures below 100 °C during the Cretaceous, when the atmospheric CO_2 concentration was higher than at present (Alt and Teagle, 1999; Staudigel et al., 1989). Note, the results from the reaction path calculations at 25 and 100 °C for the seawater system suggest the mineralization of CO_2 via the precipitation of mainly calcite, but also some ankerite (**Figures 5 and 6**, **h**). Coogan and Gillis (2013) suggested that the higher CO_2 content in Cretaceous seawater led to an enhanced alkalinity production during fluid-rock reaction in the oceanic crust, allowing for substantially more CO_2 to be taken up as calcite, similarly to what has been suggested during the injection of CO_2-charged freshwater at Hellisheiði (Clark et al., 2020). Studies of hydrothermally altered reservoirs also demonstrate that in seawater charged with up to ~6 bar $p\mathrm{CO}_2$, such as in Reykjanes, Iceland, calcite contents can reach ~13 wt% (Freedman et al., 2009; Wiese et al., 2008).

4.2. Effect of dissolved gas injection on reacted rock volume changes

Water-basalt interaction in natural systems, even without any added gases, generates significant rock volume changes. The addition of gases to the injected fluid enhances the physical and chemical alteration of primary basalt, as observed in field and modelling studies (e.g., Snæbjörnsdóttir et al., 2018a; Thien et al., 2015). Changes in rock volume determined for each reaction path system in the more dilute gas calculations corresponds to the response of the water-rock system to the dissolution of 0.2 mol of basaltic glass into 1 kg of gas-charged water over time and distance. The relative effect of gas injection on reservoir rock volume changes was estimated by comparing model outputs from corresponding gas-charged and gas-free injection calculations (see **Appendix B**). The results of such a comparison are shown in **Figure 8**.

A notably higher final rock volume change is predicted for gas-charged freshwater injection compared to gas-free freshwater injection at all temperatures except for 170 °C. In contrast, the addition of gas to seawater leads to significantly higher rock volume changes only at 25 °C. At 100 °C, the rock volume change in response to the gas-free seawater injection is comparable to that observed in response to the gas-charged seawater injection

(12% and 14%, respectively). This result is due to the decreased formation of zeolites minerals in the latter case. At 170 and 260 °C, lower rock volume changes are predicted for the gas-charged seawater injection compared to the gas-free seawater injection due to the decreased precipitation of voluminous kaolinite, Na-zeolite and chlorite in the presence of CO_2 and H_2S. At 260 °C, more chlorite precipitation is calculated to occur during the injection of seawater compared to the injection of freshwater leading to a larger increase in rock volume in the former. On the other hand, smaller rock volume changes are observed during gas-charged seawater injection compared to gas-charged freshwater injection at temperatures ≤170 °C. It should also be noted that during all the gas-charged injections other than gas-charged seawater at 260 °C a negligible change (<3%) to the rock volume is predicted during the dissolution of the first 0.02 mol of basaltic glass, which limits the risk of clogging in the proximity of the injection well.

4.3. Effects of reservoir temperature on injected gas mineralization

A comparison of the model results from the more dilute gas calculations shows that the secondary phase mineralogy, and thus the mineralization of DIC and DS, varies as a function of temperature. At 260 °C, the majority of aqueous Ca is consumed by epidote and prehnite, as well as anhydrite in the case of the seawater systems, while most aqueous Ca is consumed by carbonate formation at lower temperatures, leading to more efficient DIC mineralization. The amount of H_2S-mineralization does not change substantially with temperature, with calculations showing that even at 25 °C, most of the added DS from the injected gas-charged fluid is mineralized after no more than 0.2 mol/kgw of basaltic glass dissolution. In addition to H_2S storage, a generally increasing desulfurization trend is observed during gas-charged seawater injection as a function of increasing temperature; the amount of sulfate originally contained in the seawater fixed by mineral reactions increases from 20 to 100% with increasing temperature from 25 to 260 °C. This sulfate removal is due to both redox reactions and precipitation of anhydrite (see Section 4.4).

In the 260 °C systems, chlorite minerals were allowed to precipitate during the calculations rather than smectite. Note, however, that there is an ongoing debate surrounding smectite formation temperatures and stabilities, with some experimental observations suggesting smectite formation at temperatures as high as at 300 °C in the presence of seawater (Seyfried and Bischoff, 1979; Seyfried and Bischoff, 1981; Voigt et al., 2018b). One possibility is that smectite is a meta-stable phase at these (and even lower) temperatures and slowly transforms to mixed-layer clays, and eventually to chlorite (Schiffman and Fridleifsson, 1991). The formation of clays and zeolites is pervasive at temperatures below 260 °C, and the precipitation of these minerals consumes pore space, increasing the potential of clogging flow paths in the reservoir at some distance from the injection well, but, leaves Ca available in solution for carbon mineralization.

All calculations suggest that lower temperatures mineralize the injected carbon and sulfur more efficiently, as fewer Ca-bearing non-carbonate minerals and fewer Fe-bearing non-sulfide minerals form (**Figure 9**). However, as illustrated in **Figure 9c**, reaction rates change dramatically with temperature. Based on the activation energy of 25.5 kJ/mol (Gislason and Oelkers, 2003), and the Arrhenius (1889) equation, the basaltic glass dissolution is estimated to proceed at rates almost two orders of magnitude slower at 25 °C than at 260 °C. As such, almost two orders of magnitude more reaction time might be required for the same mass of basalt to dissolve at the lower temperature. Therefore, at low temperatures, slow reaction kinetics will have to be compensated by longer flow paths or slower flow rates than at higher temperatures for the complete mineralization of the injected gases.

4.4. Effects of fluid composition on injected gas mineralization.

The calculations presented above for different fluid compositions (**Figures 3-6**) suggest that the efficiency of gas-charged seawater carbon mineralization is somewhat lower than that of freshwater for temperatures ≥170 °C, but similar for temperatures ≤100 °C at the lower considered initial DIC concentration. For example, at 260 and 170 °C, to reach the same amount of CO_2 mineralization obtained during the gas-charged freshwater injection due the dissolution of 0.2 mol/kgw of basaltic glass requires 0.36 and 0.22 mol/kgw of basaltic glass dissolution during the gas-charged seawater injection, respectively. At temperatures ≥170 °C, the mineralization of DIC within carbonates in the presence of seawater is slowed because of extensive early anhydrite formation decreasing the Ca availability for carbonate mineral formation. This upper temperature limit for gas-charged seawater injection can be further constrained by experimental observations of significant amounts of anhydrite when heating seawater to temperatures above 150 °C (Bischoff and Seyfried, 1978). At temperatures ≤100 °C, DIC mineralization is calculated to be similar for both injected fluids in response to the dissolution of 0.2 mol/kgw basaltic glass, although the calculations suggest somewhat different pH evolutions. In the presence of seawater, the system pH is buffered at pH ≤6 due to enhanced clay mineral precipitation. As carbonate formation is expected to begin at pH approaching neutrality, depending on the temperature, the time required for the system to increase the pH towards more alkaline conditions might slow DIC mineralization somewhat in the presence of seawater. The early formation of Mg-chlorite at 260 °C, and clay minerals at temperatures ≤170 °C are the main processes buffering the pH in the presence of seawater due to the production of H^+ associated with their precipitation. The precipitation of these minerals, therefore, could slow the onset of the Ca-carbonate precipitation. This is qualitatively similar to what has been observed during some CO_2- and H_2S-free seawater-basalt interaction experiments (Seyfried and Bischoff, 1977; 1979; 1981; Voigt et al., 2018b). In these experiments the pH initially drops, most likely due to the formation of hydrated silicates.

The efficiency of DS mineralization in response to seawater injection is predicted to be similar to that of freshwater at ≥170 °C, but lower at 100 °C or below (**Figures 3-6**). Note, however, the total initial DS in the gas-charged seawater includes the sulfur naturally present in seawater itself as sulfate. Almost all of the dissolved H_2S is mineralized during the seawater injection at both 25 and 100 °C, in each case requiring the dissolution of only 0.08 mol/kgw basaltic glass. On the other hand, most of the sulfate in the seawater is removed by anhydrite precipitation at temperatures ≥170 °C, and only up to 10% by sulfate reduction reactions (**Figure 10**). Several factors influence the reduction of seawater sulfate in the modelled system as this process depends on ferrous iron, proton, and sulfate availability according to

$$8\mathrm{Fe}^{2+}_{basalt} + 9H^{+} + SO_4^{2-} = 8\mathrm{Fe}^{3+}_{basalt} + HS^{-} + 4H_2O \qquad (3)$$

where $\mathrm{Fe}^{2+}_{basalt}$ and $\mathrm{Fe}^{3+}_{basalt}$ correspond to the aqueous ferrous and ferric ions, respectively, released by the dissolution of the basaltic glass.

The H^+ required for this reaction in natural hydrothermal systems has been attributed to Mg-silicate formation reactions in previous experimental studies (e.g., Shanks et al., 1981). In the reaction path calculations presented in this study, the formation of Mg-bearing phases does not always provide sufficient protons to allow the completion of reaction (3). In addition to H^+ availability, seawater sulfate reduction can proceed only if sufficient oxidizable ferrous iron is released from the basalt as 8 Fe^{2+} are required to be oxidized to reduce one S^{6+}. Furthermore, the early precipitation of anhydrite and its separation from the flowing fluids limits sulfate reduction in the model calculations performed for gas-charged seawater-basalt interaction at 260 °C (**Figure 10**). Finally, the greater reduction potential of ferric iron compared to that of sulfate leads to the oxidation of some H_2S in response to the release of Fe^{3+} from the basalt, as can be seen in the initial reaction steps shown in **Figure 10**. The associated oxidation of sulfide into sulfate is observed at every considered temperature until less than at least 1 mmol/kgw of H_2S is left in the aqueous solution after which the reverse redox reaction start to take place, in accord with **Eqn. 3**. Due to mass balance considerations, 0.47 mmol/kg sulfate reduction is calculated for each 0.02 mol/kgw of basaltic glass dissolved, assuming that all the iron in basalt is available as ferrous iron and no Fe^{2+}-rich solid phase forms. The kinetics of the Fe-S redox reaction, however, may be a limiting factor for this process. As described by Ohmoto and Lasaga (1982) and Shanks et al. (1981), inorganic sulfate reduction rates are fast enough to become detectable and geochemically important only at temperatures above 200 °C.

The injected fluid composition also affects the rock volume increase due to the coupled dissolution-precipitation reactions in the lower considered DIC concentration systems as shown in **Figure 9b**. At 260 °C, the rock volume increase during gas-charged seawater injection is larger than that estimated for gas-charged freshwater injection due to the formation of both chlorite and anhydrite. At 170 and 100 °C, a significantly smaller rock volume increase is calculated for the seawater injection compared to the freshwater injection. This latter difference stems from the enhanced precipitation of zeolites during the freshwater injection. In contrast to the results at higher temperatures, reactions at 25 °C in response to seawater injection led to a similar rock volume increase compared to the corresponding freshwater injection. Note that most of the rock volume increases take place after substantial basalt dissolution occurs, likely avoiding flow path clogging near the injection well (**Figures 3-6 k and** l).

4.5. Effects of CO_2 concentration on mineralization

Calculations of basaltic glass interaction with fluids charged with higher CO_2 concentrations were run to provide insight into applying the CarbFix method to other gas emitting industries, such as coal, gas-fired, and oil-fired power plants (Kagel and Gawell, 2005; U.S. Environmental Protection Agency, 2010; Xu et al., 2003). The CO_2 concentrations for the injection fluids considered in these calculations were those equal to the fluid at equilibrium with 9 bar CO_2 and the injecting pressure at the well head of Hellisheiði (Clark et al., 2020).

No significant change in carbonate mineralogy was observed due to the increasing fluid pCO_2, with Ca-carbonate being the dominant CO_2-bearing precipitating mineral phase. This is in agreement with several experimental and modelling studies (e.g., Gysi and Stefánsson, 2012c; Rosenbauer et al., 2012; Sturmer et al., 2020). These studies showed that the precipitation of Mg- and Fe-carbonates occurs *i*) from fluids with pCO_2 higher than 25 bar, and *ii*) in presence of Mg-rich silicates such as olivine.

Relatively efficient CO_2-mineralization is found in all CO_2-rich freshwater and seawater model calculations for temperatures ≤170 °C, with only 0.4 mol/kgw of basaltic glass required to mineralize the CO_2 contained in these more gas-concentrated fluids (**Figure 7**). Note, however, the time required for this carbonation will depend strongly on the mineral reaction kinetics, which are not considered in these calculations. Given that the reaction path calculations do not consider reaction rates, pH higher than 10 was also reached (**Figure 7**) due to zeolite and clay minerals precipitation (**Equations 1 and 2**). The observation of such high pH is uncommon in natural systems and as suggested above is due to the precipitation of zeolites and clay minerals at extremely alkaline conditions in the model calculations. Such computed results may be an effect of the uncertainty on the thermodynamic properties of sheet silicates (Voigt et al., 2018a).

Both freshwater experiments (Gysi and Stefánsson, 2012c) and observations of basalt-hosted petroleum reservoirs in the presence of brines (Rogers et al., 2006) suggested that the mineralization of CO_2 at temperatures <100 °C was favoured by the formation of a number of different carbonate minerals, including calcite, ankerite, and magnesite. The formation of these carbonates in nature apparently stems from the formation of amorphous silica instead of the zeolites and smectites seen in the model calculations. The formation of these latter minerals may be inhibited kinetically at some conditions. To assess this possibility, CO_2-rich reaction path calculations were run at 100 °C in both freshwater and seawater systems without allowing zeolites and smectites to form. The results of these additional calculations shows that amorphous silica is expected to form in the absence of Ca-zeolites formation. Similarly, slow precipitation kinetics may explain the absence of epidote in high pCO_2 laboratory experiments (e.g., Gysi and Stefánsson, 2012c; Shibuya et al., 2013), as the reactive path calculations suggest epidote precipitation at 260 °C in response to CO_2-rich water injections. Also, based on the study of relatively fresh and strongly altered Archean basaltic rocks, Nakamura and Kato (2004) suggested that the absence of Ca-Al silicate minerals such as epidote and actinolite in strongly altered rocks was due to the continued presence of CO_2-rich hydrothermal fluids inhibiting their growth. The absence and/or delayed formation of epidote and Ca-zeolites would favour the carbon mineralization as more Ca would be available in the fluid phase to form Ca-carbonate minerals.

5. SUMMARY AND CONCLUSIONS

Reaction path model calculations were used in this study to assess the potential use of gas-charged seawater injection into basalts for subsurface CO_2 and H_2S mineralization. The model calculations were validated by the comparison of model results for gas-charged freshwater-basalt interaction at 260 °C with major elemental concentrations, mineralization percent of DIC and DS, and secondary mineral assemblages observed from the ongoing CarbFix2 injection. The results of the reaction path calculations presented above suggest that:

- 260 °C or higher temperatures are not optimal for carbon mineralization, in particular when injecting gas-charged seawater: i) relatively more basaltic glass dissolution is necessary compared to lower temperatures to increase the pH sufficiently to enable CO_2 mineralization, and ii) early anhydrite formation consumes most of the Ca available in the solution and increases the risk of clogging near the injection well in seawater systems;
- Below 260 °C, most Ca is predicted to be consumed by carbonate minerals, i.e. used for mineralization of CO_2 (mainly as calcite and in some cases ankerite);
- For gas-charged freshwater injections, the best conditions for the subsurface mineralization are at temperatures between 25 and 170 °C, where high degrees of CO_2 and H_2S mineralization have been predicted;
- For gas-charged seawater injection, the upper temperature limit for the mineral carbonation process is likely dictated by the anhydrite thermal stability field (which is above ~150 °C), below which the efficient mineralization of CO_2 and H_2S is observed.

Overall, these results indicate that the main limiting factor constraining mineral carbonation at high temperatures is the competition of secondary minerals for Ca, the main cation required for DIC mineralization, whereas at low temperatures the formation of silicate phases can uptake a significant portion of pore space within the potential reservoir. Calculations performed for the injection of more CO_2 concentrated fluids found that the injection of CO_2-rich freshwater was more efficient for carbon mineralization than CO_2-rich seawater at 260 °C, but similar efficiencies were found for temperatures ≤170 °C. At these lower temperatures, however, the fluid chemistry reaction pathway of the CO_2-rich freshwater injection differs from that of the CO_2-rich seawater. In the seawater systems, the pH is buffered at ≤6 for substantial time due to clay mineral formation, which may lead to somewhat slower carbonation rates.

Key factors controlling the rates of carbon storage via mineralization will likely be a) the rates of basalt dissolution and secondary mineral precipitation, which at 25 °C is likely around two orders of magnitude lower than at 260 °C, and b) the possible absence of zeolites and clay minerals in the presence of high pCO_2 fluids, which could favour an earlier precipitation of carbonates.

The mineralization of sulfate injected into the subsurface during gas-charged seawater injections can be influenced by oxidation-reduction reactions. Five major factors influencing this redox process were identified: i) availability of H^+, added to the fluid by Mg-phase precipitation; ii) availability of Fe^{2+}, associated with the basalt dissolution; iii) availability of sulfate, associated with the early anhydrite precipitation; iv) presence of H_2S in the fluid phase; and v) rate of Fe-S redox reactions relative to the rates of Fe^{2+}-rich secondary phases. Calculations suggested that the highest degree of sulfate reduction occurs at 170 °C, mainly due to a relatively low amount of anhydrite precipitation compared to higher temperatures, and to a higher availability of Fe^{2+} compared to lower temperatures, where several other Fe^{2+}-rich secondary phases are predicted to form.

It should be noted that all the reaction path models presented in this study were run assuming local geochemical equilibrium of the precipitated phases. Such may be only partly achieved in real systems, as reaction kinetics may play a role, particularly at lower temperatures. Nevertheless, the highest carbon and sulfur mineralization potential seems to lie at temperatures ≤170 °C, warranting investigations of the rates of carbonation reactions at these conditions.

Most significantly, the results of this study suggest that the carbonation of gas-charged seawater may be in many cases as efficient as the carbonation of gas-charged freshwater. As the CarbFix approach requires substantial quantities of water for injection, the successful mineralization of CO_2-charged seawater will extend this method's applicability. For example, submarine basalts as well as large igneous provinces (Snæbjörnsdóttir et al., 2020) nearby the coast could be suitable reservoirs for additional pilot injections using this approach.

Acknowledgements

We thank Editor Charles Jenkins, Daniel Sturmer, and the anonymous reviewer for their constructive comments that have improved the paper. This work is part of the CarbFix project and has received funding from the European Union's Horizon 2020 research and innovation programme under grant agreement No. 764760. We also thank Thomas Ratouis and the whole Reykjavik Energy-Carbfix team for providing technical feedback and access to drilling reports during the article preparation.

Appendix A

Results of reaction path calculations with CO_2-rich fluids at 25 (Fig. A1), 100 (Fig. A2), 170 (Fig. A3), and 260 °C (Fig. A4) of pH, mineralized proportion of DIC and DS, cumulative secondary mineral abundance per kg of injected fluid, Ca distribution, cumulative total volume of minerals per kg of injected fluid and their volume change for freshwater (left) and seawater (right) injections.

Appendix B

Results of reaction path calculations with gas-free fluids at 25 (Fig. B1), 100 (Fig. B2), 170 (Fig. B3), and 260 °C (Fig. B4) of pH, mineralized proportion of DIC and DS, cumulative secondary mineral abundance per kg of injected fluid, Ca distribution, cumulative total volume of minerals per kg of injected fluid and their volume change for freshwater (left) and seawater (right) injections.

References

Alfredsson, H.A., Oelkers, E.H., Hardarsson, B.S., Franzson, H., Gunnlaugsson, E., Gislason, S.R., 2013. The geology and water chemistry of the Hellisheidi, SW-Iceland carbon storage site. International Journal of Greenhouse Gas Control 12, 399-418.

Alt, J.C., 1995. Subseafloor processes in mid-ocean ridge hydrothermal systems. Seafloor Hydrothermal Systems: Physical, chemical, biological, and geological interactions, 85-114.

Alt, J.C., Kinoshita, H., Stokking, L.B., Allerton, Bach, Becker, K., Boehm, Brewer, Dilek, Filice, Fisk, Fujisawa, Fumes, Querin, Harper, Honnorez, Hoskins, Ishizuka, Laveme, McNeill, Magenheim, Miyashita, Pezard, Salisbury, Tartarotti, H., T.D.A., Vanko, Wilkens, Worm, 1996. Proc. ODP, Sci. Results, 148, Ocean Drilling Program, College Station, TX.

Alt, J.C., Teagle, D.A.H., 1999. The uptake of carbon during alteration of ocean crust. Geochimica et Cosmochimica Acta 63, 1527-1535.

Appelo, C.A.J., Parkhurst, D.L., Post, V.E.A., 2014. Equations for calculating hydrogeochemical reactions of minerals and gases such as CO_2 at high pressures and temperatures. Geochimica et Cosmochimica Acta 125, 49-67.

Arrhenius, S., 1889. About the heat of dissociation and the influence of temperature on the degree of dissociation of electrolytes. J. Phys. Chem. 4, 96-116.

Bader, M.S.H., 2007. Sulfate removal technologies for oil fields seawater injection operations. Journal of Petroleum Science and Engineering 55, 93-110.

Bischoff, J.L., Seyfried, W.E., 1978. Hydrothermal chemistry of seawater from 25 degrees to 350 degrees C. American Journal of Science 278, 838-860.

Blounot, C.W., Dickson, F.W., 1969. The solubility of anhydrite ($CaSO_4$) in NaCl-H_2O from 100 to 450°C and 1 to 1000 bars. Geochimica et Cosmochimica Acta 33, 227-245.

Clark, D.E., Gunnarsson, I., Aradóttir, E.S., Þ. Arnarson, M., Þorgeirsson, Þ.A., Sigurðardóttir, S.S., Sigfússon, B., Snæbjörnsdóttir, S.Ó., Oelkers, E.H., Gíslason, S.R., 2018. The chemistry and potential reactivity of the CO_2-H_2S charged injected waters at the basaltic CarbFix2 site, Iceland. Energy Procedia 146, 121-128.

Clark, D.E., Oelkers, E.H., Gunnarsson, I., Sigfússon, B., Snæbjörnsdóttir, S.Ó., Aradóttir, E.S., Gíslason, S.R., 2020. CarbFix2: CO_2 and H_2S mineralization during 3.5 years of continuous injection into basaltic rocks at more than 250 °C. Geochimica et Cosmochimica Acta 279, 45-66.

Coggon, R.M., Teagle, D.A.H., Cooper, M.J., Vanko, D.A., 2004. Linking basement carbonate vein compositions to porewater geochemistry across the eastern flank of the Juan de Fuca Ridge, ODP Leg 168. Earth and Planetary Science Letters 219, 111-128.

Coogan, L.A., Gillis, K.M., 2013. Evidence that low-temperature oceanic hydrothermal systems play an important role in the silicate-carbonate weathering cycle and long-term climate regulation. Geochemistry, Geophysics, Geosystems 14, 1771-1786.

Dai, Z., Kan, A.T., Shi, W., Zhang, N., Zhang, F., Yan, F., Bhandari, N., Zhang, Z., Liu, Y., Ruan, G., 2017. Solubility measurements and predictions of gypsum, anhydrite, and calcite over wide ranges of temperature, pressure, and ionic strength with mixed electrolytes. Rock Mechanics and Rock Engineering 50, 327-339.

Daval, D., 2018. Carbon dioxide sequestration through silicate degradation and carbon mineralisation: promises and uncertainties. npj Materials Degradation 2, 11.

Davis, E.E., Mottl, M.J., Fisher, A.T., Firth, J.V., 1997. Proc. ODP, Init. Repts., 168, 470 pp., Ocean Drilling Program, College Station, TX.

Fisher, A.T., Tsuji, T., Petronotis, K., the Expedition 327 Scientists, 2011. *Proc.* IODP, 327: Tokyo (Integrated Ocean Drilling Program Management International, Inc.).

Franzson, H., Zierenberg, R., Schiffman, P., 2008. Chemical transport in geothermal systems in Iceland. Journal of Volcanology and Geothermal Research 173, 217-229.

Freedman, A.J.E., Bird, D.K., Arnórsson, S., Fridriksson, T., Elders, W.A., Fridleifsson, G.Ó., 2009. Hydrothermal minerals record CO_2 partial pressures in the Reykjanes geothermal system, Iceland. American Journal of Science 309, 788-833.

Galeczka, I., Wolff-Boenisch, D., Oelkers, E.H., Gislason, S.R., 2014. An experimental study of basaltic glass–H_2O–CO_2 interaction at 22 and 50°C: Implications for subsurface storage of CO_2. Geochimica et Cosmochimica Acta 126, 123-145.

Gillis, K.M., Coogan, L.A., 2011. Secular variation in carbon uptake into the ocean crust. Earth and Planetary Science Letters 302, 385-392.

Gislason, S.R., Oelkers, E.H., 2003. Mechanism, rates, and consequences of basaltic glass dissolution: II. An experimental study of the dissolution rates of basaltic glass as a function of pH and temperature. Geochimica et Cosmochimica Acta 67, 3817-3832.

Gislason, S.R., Oelkers, E.H., 2014. Carbon storage in basalt. Science 344, 373-374.

Goldberg, D.S., Takahashi, T., Slagle, A.L., 2008. Carbon dioxide sequestration in deep-sea basalt. Proceedings of the National Academy of Sciences 105, 9920.

Gudbrandsson, S., Wolff-Boenisch, D., Gislason, S.R., Oelkers, E.H., 2011. An experimental study of crystalline basalt dissolution from $2 \leqslant pH \leqslant 11$ and temperatures from 5 to 75 °C. Geochimica et Cosmochimica Acta 75, 5496-5509.

Gunnarsson, I., Aradóttir, E.S., Oelkers, E.H., Clark, D.E., Arnarson, M.Þ., Sigfússon, B., Snæbjörnsdóttir, S.Ó., Matter, J.M., Stute, M., Júlíusson, B.M., Gíslason, S.R., 2018. The rapid and cost-effective capture and subsurface mineral storage of carbon and sulfur at the CarbFix2 site. International Journal of Greenhouse Gas Control 79, 117-126.

Gysi, A.P., Stefánsson, A., 2008. Numerical modelling of CO_2-water-basalt interaction. Mineralogical Magazine 72, 55-59.

Gysi, A.P., Stefánsson, A., 2011. CO_2–water–basalt interaction. Numerical simulation of low temperature CO_2 sequestration into basalts. Geochimica et Cosmochimica Acta 75, 4728-4751.

Gysi, A.P., Stefánsson, A., 2012a. CO_2-water–basalt interaction. Low temperature experiments and implications for CO_2 sequestration into basalts. Geochimica et Cosmochimica Acta 81, 129-152.

Gysi, A.P., Stefánsson, A., 2012b. Experiments and geochemical modeling of CO_2 sequestration during hydrothermal basalt alteration. Chemical Geology 306-307, 10-28.

Gysi, A.P., Stefánsson, A., 2012c. Mineralogical aspects of CO_2 sequestration during hydrothermal basalt alteration — An experimental study at 75 to 250°C and elevated pCO_2. Chemical Geology 306-307, 146-159.

Helgadóttir, H.M., 2011. The Gráuhnúkar geothermal system, Hellisheiði: Geology and hydrothermal alteration. University of Iceland, p. 186.

Kagel, A., Gawell, K., 2005. Promoting geothermal energy: air emissions comparison and externality analysis. The Electricity Journal 18, 90-99.

Kanakiya, S., Adam, L., Esteban, L., Rowe, M.C., Shane, P., 2017. Dissolution and secondary mineral precipitation in basalts due to reactions with carbonic acid. Journal of Geophysical Research: Solid Earth 122, 4312-4327.

Kelemen, P.B., Matter, J.M., 2008. In situ carbonation of peridotite for CO_2 storage. Proceedings of the National Academy of Sciences 105, 17295-17300.

Kristmannsdóttir, H., 1979. Alteration of basaltic rocks by hydrothermal activity at 100-300 °C. Developments in sedimentology 27, 359-367.

Krìstmannsdóttir, H., Tomasson, J., 1978. Zeolite zones in geothermal areas in Iceland, in: Sand, L.B., Mumpton, F.M. (Eds.), Natural Zeolite Occurrence, Properties and Use. Pergamon Press, Oxford, pp. 277-284.

Langmuir, D., 1997. Aqueous Environmental Geochemistry. Prentice Hall, Upper Saddle River, NJ.

Larsson, D., Grönvold, K., Oskarsson, N., Gunnlaugsson, E., 2002. Hydrothermal alteration of plagioclase and growth of secondary feldspar in the Hengill Volcanic Centre, SW Iceland. Journal of Volcanology and Geothermal Research 114, 275-290.

Luhmann, A.J., Tutolo, B.M., Tan, C., Moskowitz, B.M., Saar, M.O., Seyfried, W.E., 2017. Whole rock basalt alteration from CO_2-rich brine during flow-through experiments at 150 °C and 150 bar. Chemical Geology 453, 92-110.

Marieni, C., Henstock, T.J., Teagle, D.A.H., 2013. Geological storage of CO_2 within the oceanic crust by gravitational trapping. Geophysical Research Letters 40, 6219-6224.

Marieni, C., Přikryl, J., Aradóttir, E.S., Gunnarsson, I., Stefánsson, A., 2018. Towards 'green' geothermal energy: Co-mineralization of carbon and sulfur in geothermal reservoirs. International Journal of Greenhouse Gas Control 77, 96-105.

Matter, J.M., Stute, M., Snæbjörnsdottir, S.Ó., Oelkers, E.H., Gislason, S.R., Aradottir, E.S., Sigfusson, B., Gunnarsson, I., Sigurdardottir, H., Gunnlaugsson, E., Axelsson, G., Alfredsson, H.A., Wolff-Boenisch, D., Mesfin, K., Taya, D.F.d.I.R., Hall, J., Dideriksen, K., Broecker, W.S., 2016. Rapid carbon mineralization for permanent disposal of anthropogenic carbon dioxide emissions. Science 352, 1312.

McGrail, B.P., Schaef, H.T., Spane, F.A., Cliff, J.B., Qafoku, O., Horner, J.A., Thompson, C.J., Owen, A.T., Sullivan, C.E., 2016. Field validation of supercritical CO_2 reactivity with basalts. Environmental Science & Technology Letters.

Metz, B., Davidson, O., de Coninck, H., Loos, M., Meyer, L., 2005. IPCC Special Report on Carbon Dioxide Capture and Storage, Cambridge University Press, UK.

Millero, F.J., Feistel, R., Wright, D.G., McDougall, T.J., 2008. The composition of standard seawater and the definition of the reference-composition salinity scale. Deep Sea Research Part I: Oceanographic Research Papers 55, 50-72.

Nakamura, K., Kato, Y., 2004. Carbonatization of oceanic crust by the seafloor hydrothermal activity and its significance as a CO_2 sink in the Early Archean. Geochimica et Cosmochimica Acta 68, 4595-4618.

Neuhoff, P.S., Fridriksson, T., Arnorsson, S., Bird, D.K., 1999. Porosity evolution and mineral paragenesis during low-grade metamorphism of basaltic lavas at Teigarhorn, eastern Iceland. American Journal of Science 299, 467-501.

Neveu, M., Desch, S.J., Castillo-Rogez, J.C., 2017. Aqueous geochemistry in icy world interiors: Equilibrium fluid, rock, and gas compositions, and fate of antifreezes and radionuclides. Geochimica et Cosmochimica Acta 212, 324-371.

Oelkers, E.H., Gislason, S.R., 2001. The mechanism, rates and consequences of basaltic glass dissolution: I. An experimental study of the dissolution rates of basaltic glass as a function of aqueous Al, Si and oxalic acid concentration at 25 C and pH= 3 and 11. Geochimica et Cosmochimica Acta 65, 3671-3681.

Oelkers, E.H., Gislason, S.R., Matter, J., 2008. Mineral carbonation of CO_2. Elements 4, 333-337.

Ohmoto, H., Lasaga, A.C., 1982. Kinetics of reactions between aqueous sulfates and sulfides in hydrothermal systems. Geochimica et Cosmochimica Acta 46, 1727-1745.

Pacala, S., Socolow, R., 2004. Stabilization wedges: Solving the climate problem for the next 50 years with current technologies. Science 305, 968-972.

Parkhurst, D.L., Appelo, C.A.J., 2013. Description of input and examples for PHREEQC version 3: a computer program for speciation, batch-reaction, one-dimensional transport, and inverse geochemical calculations. US Geological Survey.

Peng, D.-Y., Robinson, D.B., 1976. Two and three phase equilibrium calculations for systems containing water. The Canadian Journal of Chemical Engineering 54, 595-599.

Peuble, S., Godard, M., Luquot, L., Andreani, M., Martinez, I., Gouze, P., 2015. CO_2 geological storage in olivine rich basaltic aquifers: new insights from reactive-percolation experiments. Applied Geochemistry 52, 174-190.

Power, I.M., Harrison, A.L., Dipple, G.M., Wilson, S.A., Kelemen, P.B., Hitch, M., Southam, G., 2013. Carbon mineralization: from natural analogues to engineered systems. Reviews in Mineralogy and Geochemistry 77, 305-360.

Rausch, S., 2012. Carbonate veins as recorders of seawater evolution, CO_2 uptake by the ocean crust, and seawater-crust interaction during low-temperature alteration. Bremen, Universität Bremen.

Rausch, S., Böhm, F., Bach, W., Klügel, A., Eisenhauer, A., 2013. Calcium carbonate veins in ocean crust record a threefold increase of seawater Mg/Ca in the past 30 million years. Earth and Planetary Science Letters 362, 215-224.

Rogelj, J., Shindell, D., Jiang, K., Fifita, S., Forster, P., Ginzburg, V., Handa, C., Kheshgi, H., Kobayashi, S., Kriegler, E., Mundaca, L., Séférian, R., Vilariño, M.V., 2018. Mitigation Pathways Compatible with 1.5°C in the Context of Sustainable Development, in: Masson-

Delmotte, V., P. Zhai, H.-O. Pörtner, D. Roberts, J. Skea, P.R. Shukla, A. Pirani, W. Moufouma-Okia, C. Péan, R. Pidcock, S. Connors, J.B.R. Matthews, Y. Chen, X. Zhou, M.I. Gomis, E. Lonnoy, T. Maycock, M. Tignor, and T. Waterfield (Ed.), In: *Global Warming of 1.5°C. An IPCC Special Report on the impacts of global warming of 1.5°C above pre-industrial levels and related global greenhouse gas emission pathways, in the context of strengthening the global response to the threat of climate change, sustainable development, and efforts to eradicate poverty*, *In Press*.

Rogers, K.L., Neuhoff, P.S., Pedersen, A.K., Bird, D.K., 2006. CO_2 metasomatism in a basalt-hosted petroleum reservoir, Nuussuaq, West Greenland. Lithos 92, 55-82.

Rose, N.M., 1991. Dissolution rates of prehnite, epidote, and albite. Geochimica et Cosmochimica Acta 55, 3273-3286.

Rosenbauer, R.J., Thomas, B., Bischoff, J.L., Palandri, J., 2012. Carbon sequestration via reaction with basaltic rocks: Geochemical modeling and experimental results. Geochimica et Cosmochimica Acta 89, 116-133.

Sanna, A., Uibu, M., Caramanna, G., Kuusik, R., Maroto-Valer, M., 2014. A review of mineral carbonation technologies to sequester CO 2. Chemical Society Reviews 43, 8049-8080.

Schaef, H.T., McGrail, B.P., 2009. Dissolution of Columbia River Basalt under mildly acidic conditions as a function of temperature: Experimental results relevant to the geological sequestration of carbon dioxide. Applied Geochemistry 24, 980-987.

Schaef, H.T., McGrail, B.P., Owen, A.T., 2009. Basalt- CO_2–H_2O interactions and variability in carbonate mineralization rates. Energy Procedia 1, 4899-4906.

Schaef, H.T., McGrail, B.P., Owen, A.T., 2010. Carbonate mineralization of volcanic province basalts. International Journal of Greenhouse Gas Control 4, 249-261.

Schiffman, P., Fridleifsson, G.O., 1991. The smectite–chlorite transition in drillhole NJ-15, Nesjavellir geothermal field, Iceland: XRD, BSE and electron microprobe investigations. Journal of Metamorphic Geology 9, 679-696.

Seyfried, W., Bischoff, J.L., 1977. Hydrothermal transport of heavy metals by seawater: the role of seawater/basalt ratio. Earth and Planetary Science Letters 34, 71-77.

Seyfried, W.E., Bischoff, J.L., 1979. Low temperature basalt alteration by sea water: an experimental study at 70°C and 150°C. Geochimica et Cosmochimica Acta 43, 1937-1947.

Seyfried, W.E., Bischoff, J.L., 1981. Experimental seawater-basalt interaction at 300°C, 500 bars, chemical exchange, secondary mineral formation and implications for the transport of heavy metals. Geochimica et Cosmochimica Acta 45, 135-147.

Shanks, W.C., Bischoff, J.L., Rosenbauer, R.J., 1981. Seawater sulfate reduction and sulfur isotope fractionation in basaltic systems: interaction of seawater with fayalite and magnetite at 200–350 °C. Geochimica et Cosmochimica Acta 45, 1977-1995.

Shibuya, T., Tahata, M., Kitajima, K., Ueno, Y., Komiya, T., Yamamoto, S., Igisu, M., Terabayashi, M., Sawaki, Y., Takai, K., Yoshida, N., Maruyama, S., 2012. Depth variation of carbon and oxygen isotopes of calcites in Archean altered upperoceanic crust: Implications for the CO_2 flux from ocean to oceanic crust in the Archean. Earth and Planetary Science Letters 321-322, 64-73.

Shibuya, T., Yoshizaki, M., Masaki, Y., Suzuki, K., Takai, K., Russell, M.J., 2013. Reactions between basalt and CO_2-rich seawater at 250 and 350 °C, 500 bars: Implications for the CO_2 sequestration into the modern oceanic crust and the composition of hydrothermal vent fluid in the CO_2-rich early ocean. Chemical Geology 359, 1-9.

Sissmann, O., Brunet, F., Martinez, I., Guyot, F., Verlaguet, A., Pinquier, Y., Daval, D., 2014. Enhanced Olivine Carbonation within a Basalt as Compared to Single-Phase Experiments: Reevaluating the Potential of CO_2 Mineral Sequestration. Environmental Science & Technology 48, 5512-5519.

Snæbjörnsdóttir, S.Ó., Gislason, S.R., 2016. CO_2 Storage potential of basaltic rocks offshore Iceland. Energy Procedia 86, 371-380.

Snæbjörnsdóttir, S.Ó., Gislason, S.R., Galeczka, I.M., Oelkers, E.H., 2018a. Reaction path modelling of in-situ mineralisation of CO_2 at the CarbFix site at Hellisheidi, SW-Iceland. Geochimica et Cosmochimica Acta 220, 348-366.

Snæbjörnsdóttir, S.Ó., Sigfússon, B., Marieni, C., Goldberg, D., Gislason, S.R., Oelkers, E.H., 2020. Carbon dioxide storage through mineral carbonation. Nature Reviews Earth & Environment 1, 90-102.

Snæbjörnsdóttir, S.Ó., Tómasdóttir, S., Sigfússon, B., Aradottir, E.S., Gunnarsson, G., Niemi, A., Basirat, F., Dessirier, B., Gislason, S.R., Oelkers, E.H., Franzson, H., 2018b. The geology and hydrology of the CarbFix2 site, SW-Iceland. Energy Procedia 146, 146-157.

Snæbjörnsdóttir, S.Ó., Tómasdóttir, S., Sigfússon, B., Aradóttir, E.S., Gunnarsson, G., Niemi, A., Basirat, F., Dessirier, B., Gislason, S.R., Oelkers, E.H., Franzson, H., 2018c. The geology and hydrology of the CarbFix2 site, SW-Iceland. Energy Procedia 146, 146-157.

Staudigel, H., Hart, S.R., Schmincke, H.-U., Smith, B.M., 1989. Cretaceous ocean crust at DSDP Sites 417 and 418: Carbon uptake from weathering versus loss by magmatic outgassing. Geochimica et Cosmochimica Acta 53, 3091-3094.

Stefánsson, A., Arnórsson, S., Gunnarsson, I., Kaasalainen, H., Gunnlaugsson, E., 2011. The geochemistry and sequestration of H_2S into the geothermal system at Hellisheidi, Iceland. Journal of Volcanology and Geothermal Research 202, 179-188.

Sturmer, D.M., Tempel, R.N., Soltanian, M.R., 2020. Geological carbon sequestration: Modeling mafic rock carbonation using point-source flue gases. International Journal of Greenhouse Gas Control 99, 103106.

Thien, B.M.J., Kosakowski, G., Kulik, D.A., 2015. Differential alteration of basaltic lava flows and hyaloclastites in Icelandic hydrothermal systems. Geothermal Energy 3, 11.

Trias, R., Ménez, B., le Campion, P., Zivanovic, Y., Lecourt, L., Lecoeuvre, A., Schmitt-Kopplin, P., Uhl, J., Gislason, S.R., Alfreðsson, H.A., Mesfin, K.G., Snæbjörnsdóttir, S.Ó., Aradóttir, E.S., Gunnarsson, I., Matter, J.M., Stute, M., Oelkers, E.H., Gérard, E., 2017. High reactivity of deep biota under anthropogenic CO_2 injection into basalt. Nature Communications 8, 1063.

U.S. Environmental Protection Agency, 2010. Available and emerging technologies for reducing greenhouse gas emissions from the petroleum refining industry. Office of Air and Radiation. Office of Atmospheric Programs, Research Triangle Park, North Carolina, October 2010.

Voigt, M., Marieni, C., Clark, D.E., Gíslason, S.R., Oelkers, E.H., 2018a. Evaluation and refinement of thermodynamic databases for mineral carbonation. Energy Procedia 146, 81-91.

Voigt, M., Pearce, C.R., Baldermann, A., Oelkers, E.H., 2018b. Stable and radiogenic strontium isotope fractionation during hydrothermal seawater-basalt interaction. Geochimica et Cosmochimica Acta.

Wiese, F., Fridriksson, T., Ármannsson, H., 2008. CO_2 fixation by calcite in high-temperature geothermal systems in Iceland. ÍSOR, Iceland Geosurvey, Reykjavík.

Wolff-Boenisch, D., Galeczka, I.M., 2018. Flow-through reactor experiments on basalt-(sea) water-CO_2 reactions at 90 °C and neutral pH. What happens to the basalt pore space under post-injection conditions? International Journal of Greenhouse Gas Control 68, 176-190.

Wolff-Boenisch, D., Gislason, S.R., Oelkers, E.H., 2004a. The effect of fluoride on the dissolution rates of natural glasses at pH 4 and 25°C. Geochimica et Cosmochimica Acta 68, 4571-4582.

Wolff-Boenisch, D., Gislason, S.R., Oelkers, E.H., 2006. The effect of crystallinity on dissolution rates and CO_2 consumption capacity of silicates. Geochimica et Cosmochimica Acta 70, 858-870.

Wolff-Boenisch, D., Gislason, S.R., Oelkers, E.H., Putnis, C.V., 2004b. The dissolution rates of natural glasses as a function of their composition at pH 4 and 10.6, and temperatures from 25 to 74°C. Geochimica et Cosmochimica Acta 68, 4843-4858.

Wolff-Boenisch, D., Wenau, S., Gislason, S.R., Oelkers, E.H., 2011. Dissolution of basalts and peridotite in seawater, in the presence of ligands, and CO_2: implications for mineral sequestration of carbon dioxide. Geochimica et Cosmochimica Acta 75, 5510-5525.

Xu, T., Apps, J.A., Pruess, K., Yamamoto, H., 2007. Numerical modeling of injection and mineral trapping of CO_2 with H_2S and SO_2 in a sandstone formation. Chemical Geology 242, 319-346.

Xu, X., Song, C., Wincek, R., Andresen, J.M., Miller, B.G., Scaroni, A.W., 2003. Separation of CO_2 from power plant flue gas using a novel CO_2 "molecular basket" adsorbent. Fuel Chem. Div. Prepr 48, 162-163.

TABLES

Table 1. Physical and chemical properties of Stapafell basaltic glass (BG).

BG stoichiometry	$SiTi_{0.024}Al_{0.358}Fe_{0.188}Mg_{0.281}Ca_{0.264}Na_{0.079}K_{0.008}O_{3.370}$
Molecular weight	123 g/mol
Molar mass	43.158 cm^3/mol

Table 2. Freshwater (Gunnarsson et al., 2018), seawater (Millero et al., 2008), and averaged formation water (Clark et al., 2020) compositions used in the reactive path calculations. Values are given in mmol/kgw; TA stands for total alkalinity, given in meq/kgw, and DIC for dissolved inorganic carbon.

	Freshwater	**Seawater**	**Formation water**
T, °C	25	25	263
pH	8.99	8.10	7.17
TA	1.88	2.30	2.34
DIC	0.35	2.04	8.15
Al	0.05	-	0.07
Si	8.45	-	8.84
Na	6.36	486	5.83
Mg	-	54.74	-
Ca	0.01	10.66	0.02
K	0.64	10.58	0.57
H_2S	0.49	-	1.05
SO_4	0.24	29.26	0.27
Cl	3.58	566	2.89
F	0.05	0.07	0.10

Table 3. Initial fluid compositions of carbon and sulfur used for the gas-charged and CO_2-rich reaction path calculations. Total DIC and DS are the water concentrations that include injected CO_2 and H_2S, and carbon and sulfur already present in natural freshwater or seawater.

	Gas-charged freshwater	**Gas-charged seawater**	**CO_2-rich freshwater**	**CO_2-rich seawater**
Injected CO_2 (mmol/kgw)	30.6	30.6	127.0	114.4
Injected H_2S (mmol/kgw)	21.9	21.9	21.9	21.9
Total DIC (mmol/kgw)	30.8	32.0	127.2	115.8
Total DS (mmol/kgw)	22.4	42.4	22.4	42.4

Table 4. Compositions, formulas, molar volumes and thermal stability field of the secondary phases allowed to precipitate during the reaction path calculations presented in the present study.

Phase	Formula	Molar volume (cm^3/mol)	Thermal stability	Reference
Carbonates				
Ankerite	$CaFe(CO_3)_2$	66.060		
Aragonite	$CaCO_3$	34.15		
Calcite	$CaCO_3$	36.934		
Magnesite	$MgCO_3$	28.018		
Siderite	$FeCO_3$	29.378		
S-minerals				
Anhydrite	$CaSO_4$	45.94	≥100 °C	[1]
Pyrite	FeS_2	23.94		
Pyrrhotite	FeS	18.2		
Fe oxy-hydroxides				
Goethite	FeOOH	20.82		
Hematite	Fe_2O_3	30.274		
Ilmenite	$FeTiO_3$	32.15		
Magnetite	Fe_3O_4	44.524		
Titanite	$CaTiSiO_5$	55.65		
Feldspars				
Albite	$NaAlSi_3O_8$	100.25	≥250 °C	[2]
K-feldspar	$KAlSi_3O_8$	108.87	≥250 °C	[2]
Clay minerals (Smectites)				
Saponite-Fe-Fe	$Fe_{3.175}Al_{0.35}Si_{3.65}O_{10}(OH)_2$	142.672	<200 °C	[3, 4, 5, 6]
Saponite-Fe-K	$K_{0.35}Fe_3Al_{0.35}Si_{3.65}O_{10}(OH)_2$	147.639	<200 °C	[3, 4, 5, 6]
Saponite-Mg-Mg	$Mg_{3.175}Al_{0.35}Si_{3.65}O_{10}(OH)_2$	140.285	<200 °C	[3, 4, 5, 6]
Saponite-Mg-K	$K_{0.35}Mg_3Al_{0.35}Si_{3.65}O_{10}(OH)_2$	145.383	<200 °C	[3, 4, 5, 6]
Saponite-Mg-Fe	$Fe_{0.175}Mg_3Al_{0.35}Si_{3.65}O_{10}(OH)_2$	140.416	<200 °C	[3, 4, 5, 6]
Beidellite-Ca	$Ca_{0.175}Al_{2.35}Si_{3.65}O_{10}(OH)_2$	133.081	<200 °C	[3, 4, 5, 6]
Beidellite-Fe	$Fe_{0.175}Al_{2.35}Si_{3.65}O_{10}(OH)_2$	134.293	<200 °C	[3, 4, 5, 6]
Beidellite-K	$K_{0.35}Al_{2.35}Si_{3.65}O_{10}(OH)_2$	137.214	<200 °C	[3, 4, 5, 6]
Beidellite-Mg	$Mg_{0.175}Al_{2.35}Si_{3.65}O_{10}(OH)_2$	132.116	<200 °C	[3, 4, 5, 6]
Beidellite-Na	$Na_{0.35}Al_{2.35}Si_{3.65}O_{10}(OH)_2$	134.522	<200 °C	[3, 4, 5, 6]
Mica				
Celadonite	$KMgAlSi_4O_{10}(OH)_2$	157.1	≤100 °C	[3]
Chlorites				
Clinochlore	$Mg_5Al_2Si_3O_{10}(OH)_8$	207.11	>200 °C	[3, 5, 6]
Zeolites				
Analcime	$Na_{0.96}Al_{0.96}Si_{2.04}O_6{:}H_2O$	97.43	<200 °C	[2]
Chabazite-Ca	$CaAl_2Si_4O_{12}{:}6H_2O$	247.45	≤100 °C	[4]
Chabazite-Na	$Na_2Al_2Si_4O_{12}{:}6H_2O$	247.45	≤100 °C	[4]
Laumontite	$CaAl_2Si_4O_{12}{:}4.5H_2O$	209.68	100-200 °C	[4]
Mordenite-Ca	$Ca_{0.5}AlSi_5O_{12}{:}4H_2O$	208.74	80-230 °C	[7]
Stilbite-Ca	$CaAl_2Si_7O_{18}{:}7H_2O$	333.48	70-150 °C	[7]
Thomsonite	$Ca_2NaAl_5Si_5O_{20}{:}6H_2O$	338.10	≤100 °C	[4]
Wairakite	$CaAl_2Si_4O_{12}{:}2H_2O$	190.35	>180 °C	[2, 4]
Other silicates				
Epidote	$Ca_2FeAl_2Si3O_{12}OH$	139.2	>200 °C	[2, 8]
Kaolinite *	$Al_2Si_2O_5(OH)_4$	99.52		
Quartz	SiO_2	22.68	>180 °C	[5]
Amorphous silica **	SiO_2	29.00	75-150 °C	[9]
Prehnite	$Ca_2Al_2Si_3O_{10}(OH)_2$	140.33	>200 °C	[8]

[1] Blounot and Dickson (1969), [2] Larsson et al. (2002), [3] Alt (1995), [4] Kristmannsdóttir (1979), [5] Snæbjörnsdóttir et al. (2018b), [6] Schiffman and Fridleifsson (1991), [7] Krìstmannsdóttir and Tomasson (1978), [8] Rose (1991), [9] Gysi and Stefánsson (2012c)

* Only in seawater system without gases at 170 °C

** Only in systems with more concentrated CO_2 fluids

FIGURES

Figure 1. Conceptual illustration of the reaction path model structure used in PHREEQC (v3) to simulate the injection front moving away from the injection well. In total, ten reactive rock ‘boxes” of porous basaltic glass were allowed to interact with the injected fluid consecutively.

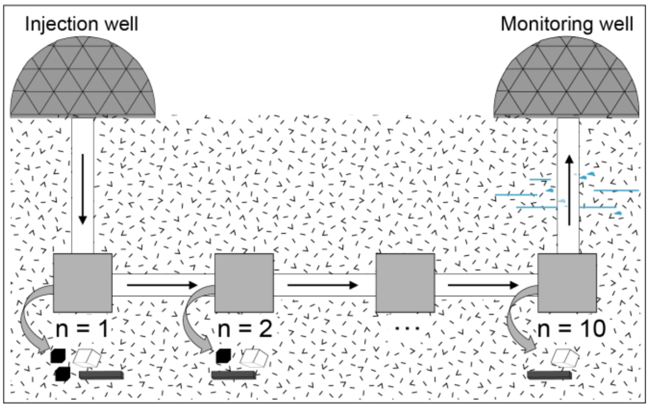

Figure 2. Comparison of selected results from the reaction path calculations at 260 °C performed to simulate the CarbFix2 system (samples collected on the *3rd of* November 2015). From top to bottom: (a) pH and (b) aqueous DIC and DS shown as a function of dissolved basaltic glass mass, (c) aqueous element concentrations, and (d) saturation indices of secondary minerals.

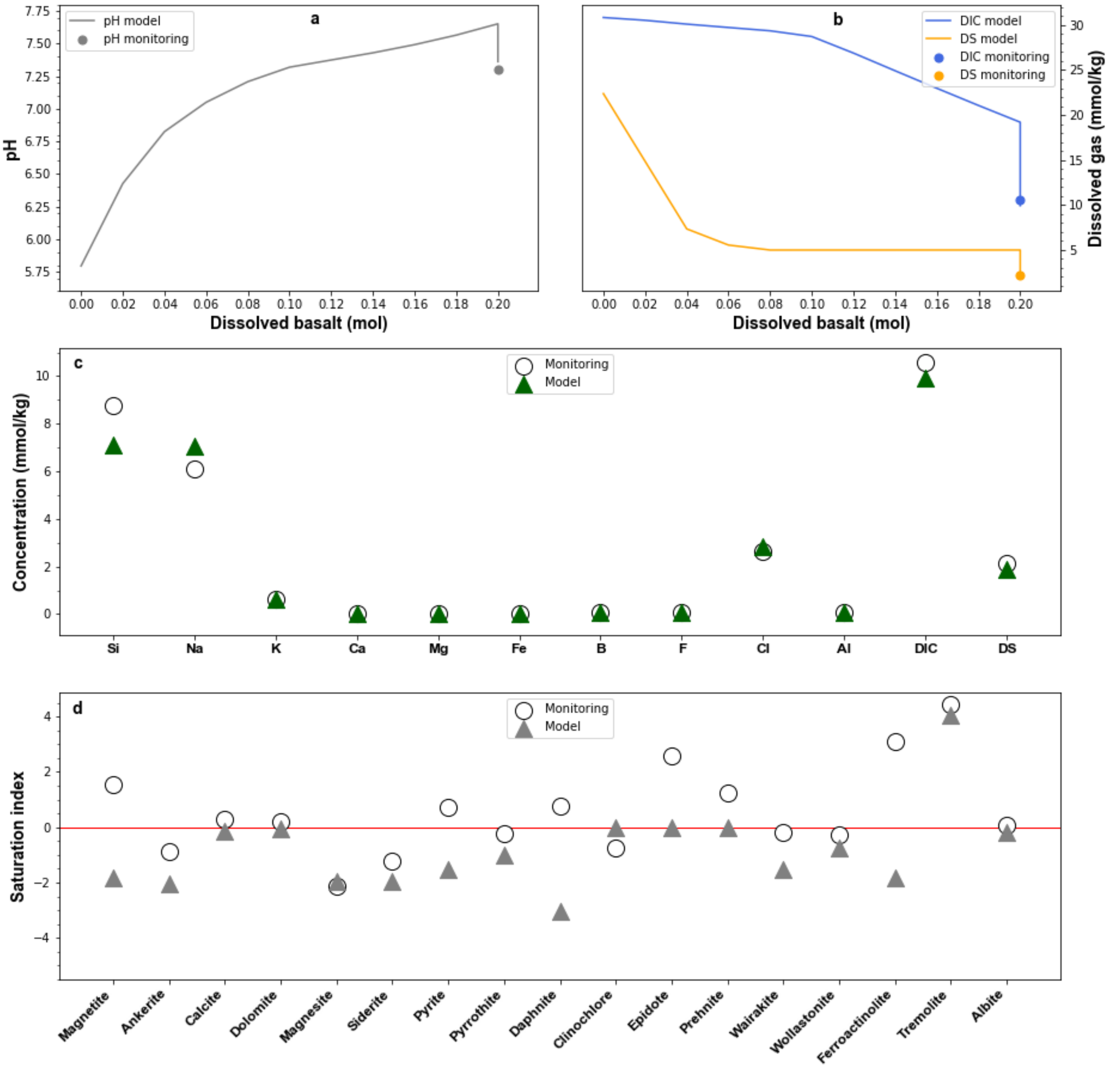

Figure 3. Reaction path calculations results of gas-charged waters at 260 °C of (a, b) pH, (c, d) mineralized proportion of DIC and DS, (e, f) cumulative secondary mineral abundance per kg of injected fluid, (g, h) Ca distribution in the precipitated secondary minerals, (i, j) cumulative total volume of minerals dissolved or precipitated per kg of injected fluid, and (k, l) their volume change for freshwater (left) and seawater (right) injections.

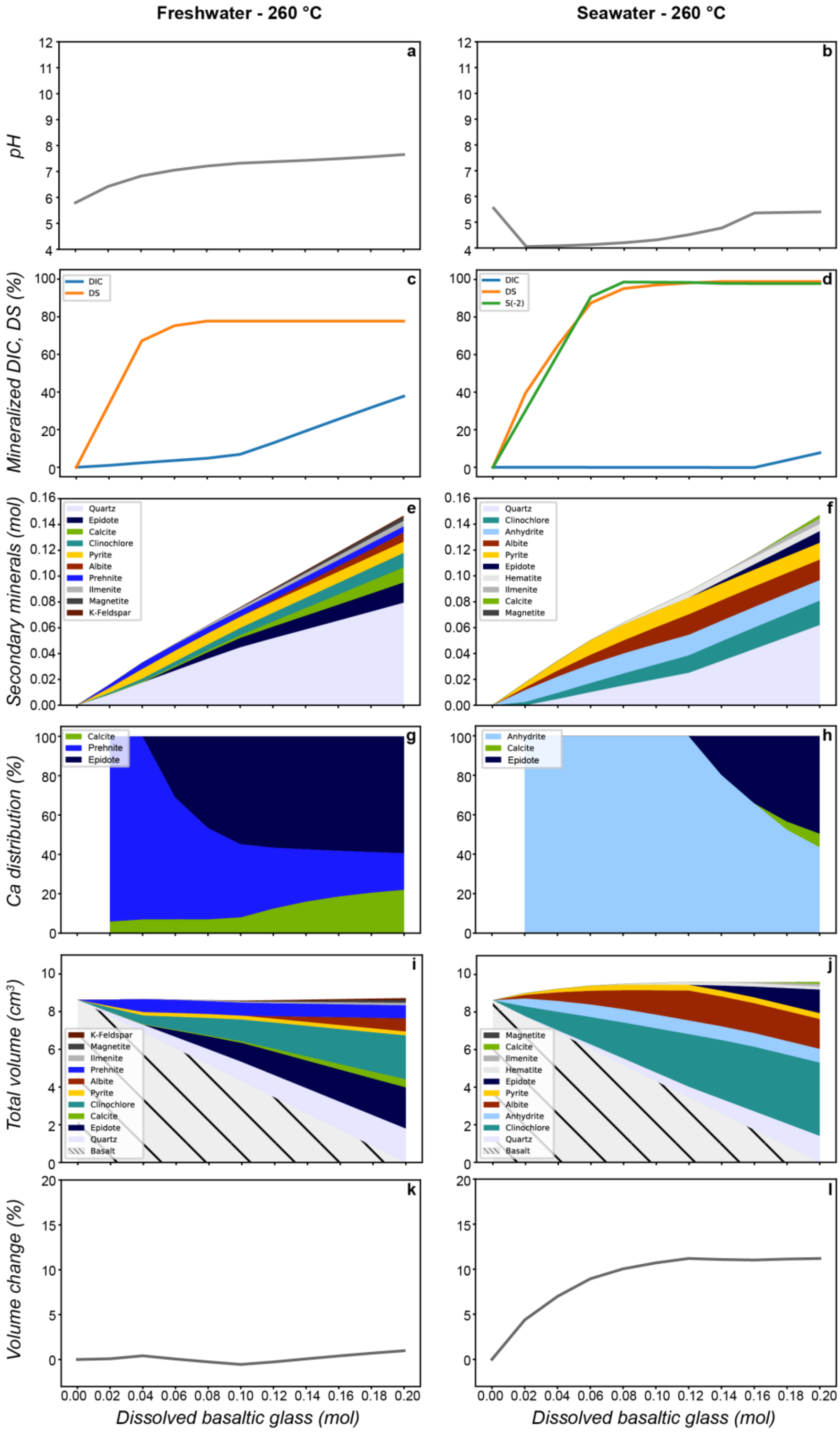

Figure 4. Reaction path calculations results of gas-charged waters at 170 °C of (a, b) pH, (c, d) mineralized proportion of DIC and DS, (e, f) cumulative secondary mineral abundance per kg of injected fluid, (g, h) Ca distribution in the precipitated secondary minerals, (i, j) cumulative total volume of minerals per kg of injected fluid and (k, l) their volume change for freshwater (left) and seawater (right) injections.

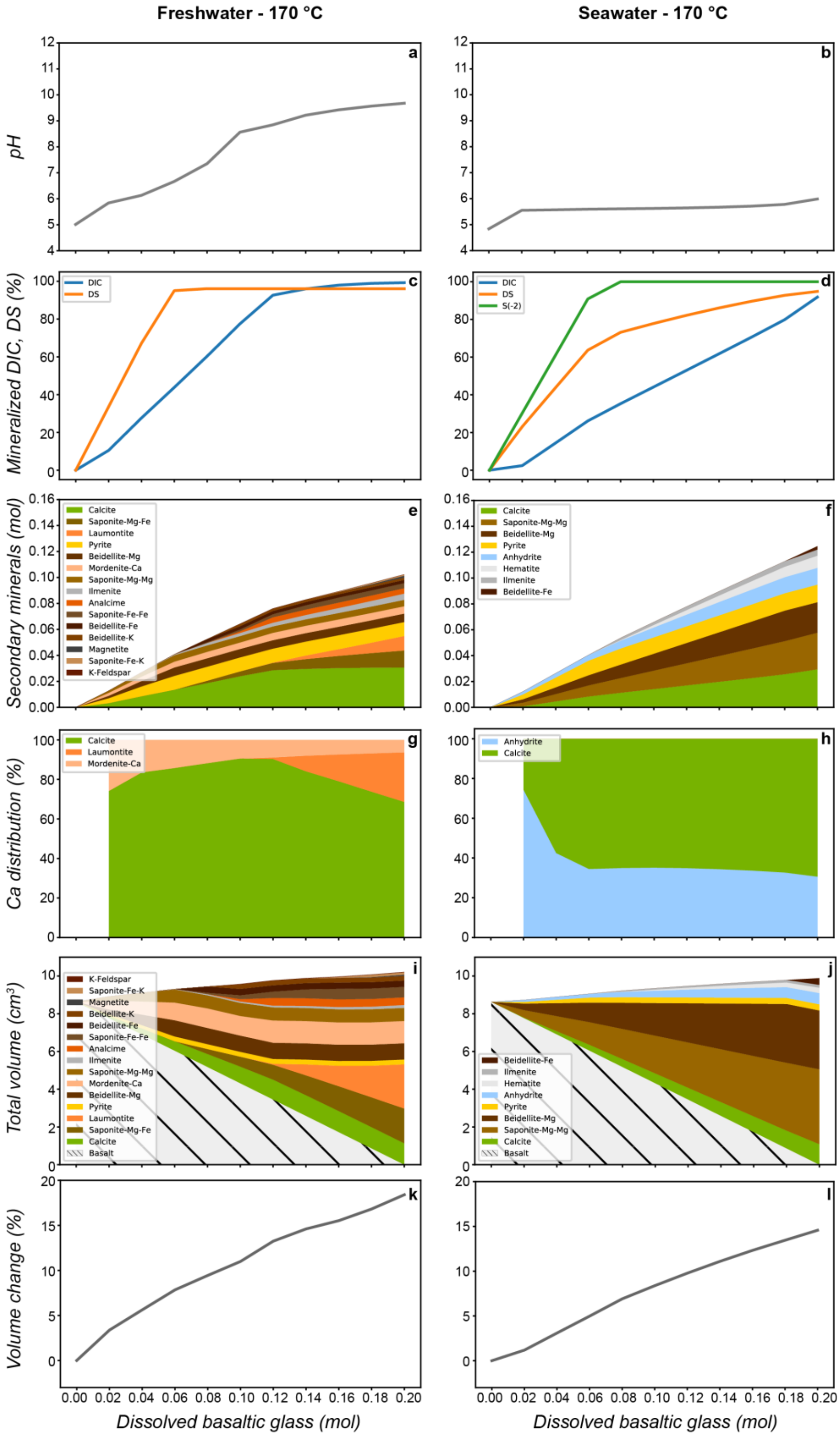

Figure 5. Reaction path calculations results of gas-charged waters at 100 °C of (a, b) pH, (c, d) mineralized proportion of DIC and DS, (e, f) cumulative secondary mineral abundance per kg of injected fluid, (g, h) Ca distribution in the precipitated secondary minerals, (i, j) cumulative total volume of minerals per kg of injected fluid and (k, l) their volume change for freshwater (left) and seawater (right).

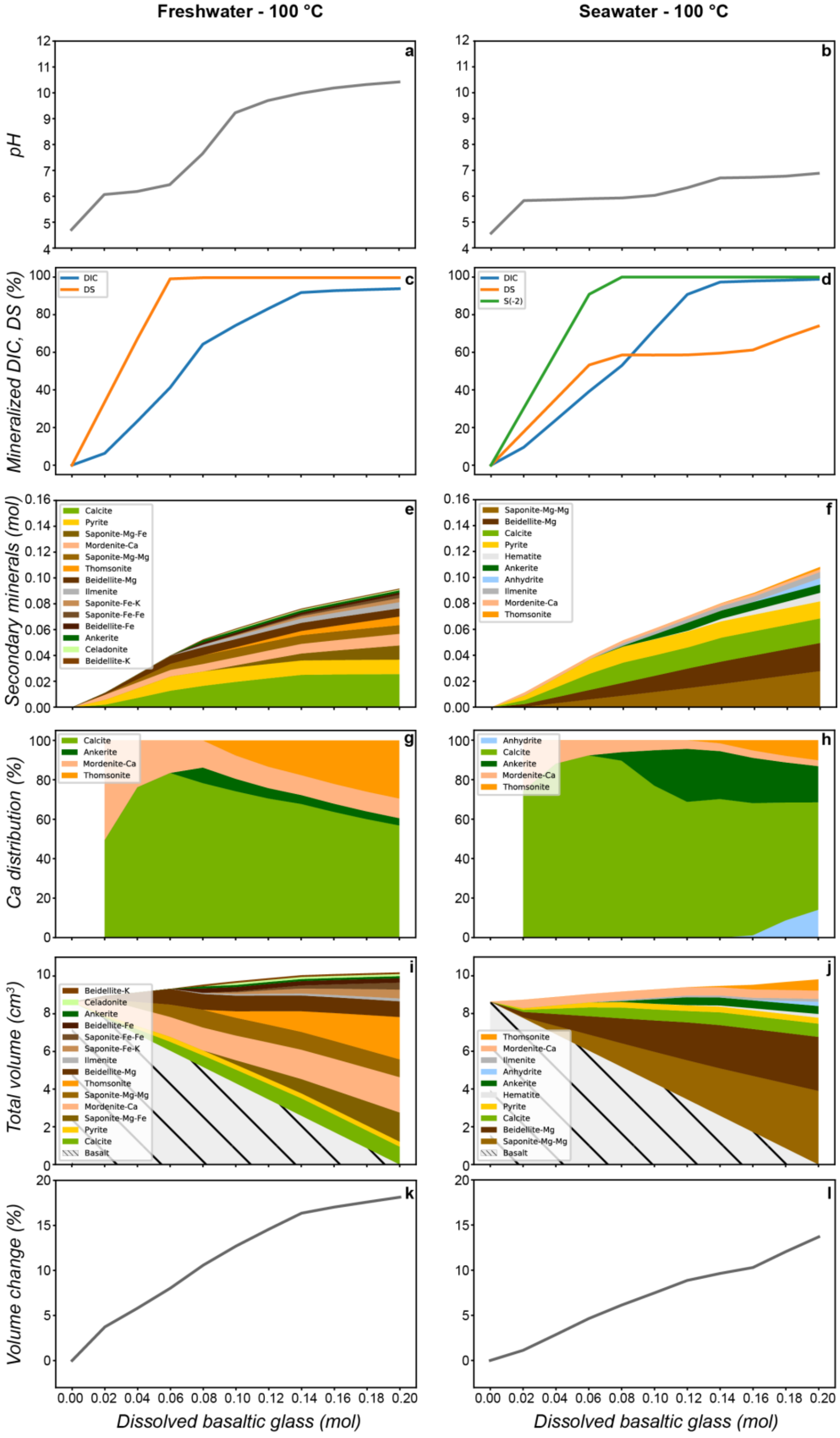

Figure 6. Reaction path calculations results of gas-charged waters at 25 °C of (a, b) pH, (c, d) mineralized proportion of DIC and DS, (e, f) cumulative secondary mineral abundance per kg of injected fluid, (g, h) Ca distribution in the precipitated secondary minerals, (i, l) cumulative total volume of minerals per kg of injected fluid and (k, l) their volume change for freshwater (left) and seawater (right).

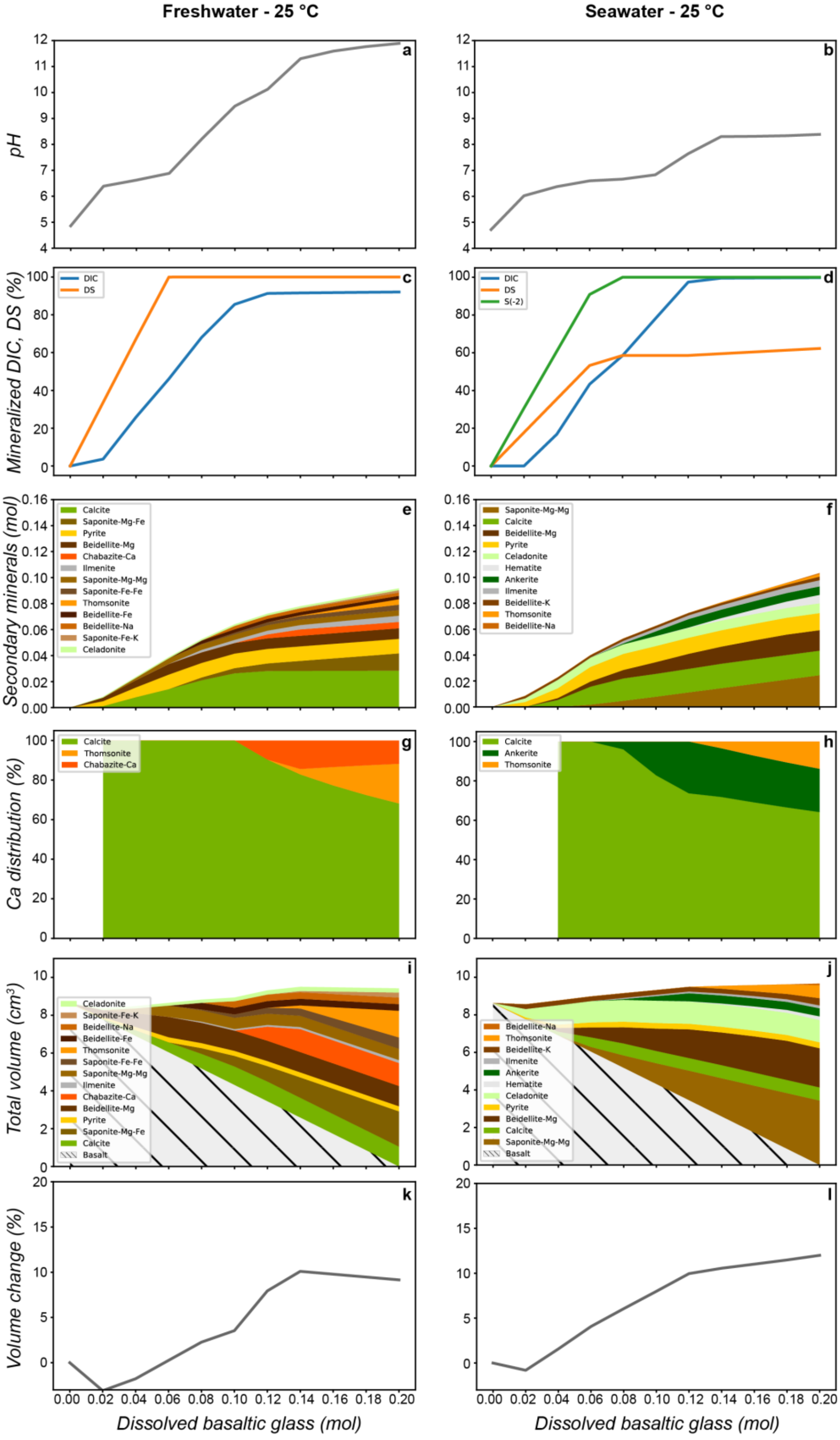

Figure 7. Results of reaction path calculations with CO_2-rich waters at temperatures from 25 to 260 °C of pH (top) and aqueous DIC (bottom) as a function of dissolved basalt mass. Results of CO_2-rich freshwater injections are shown in grey, whereas those of seawater are shown in green. Circles represent the mass of basaltic glass dissolution required to mineralize ~90% of the injected CO_2 (DIC concentration <0.012 mol/kgw). Dashed lines indicate the continuation of reaction paths once pH increased beyond 10 (see text for explanation).

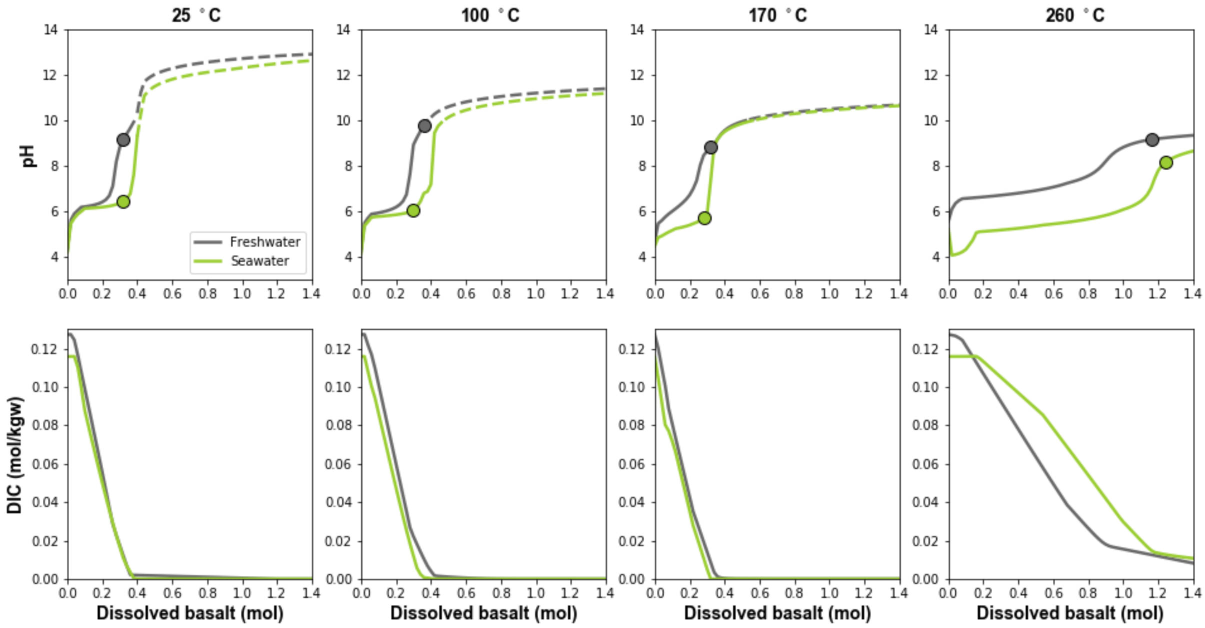

Figure 8. Calculated rock volume change in response to the dissolution and interaction of 0.2 mol of basaltic glass with freshwater and seawater as a function of temperature and gas content. The “with gas” bars represent results obtained using a gas-charged injection fluid with lower DIC concentrations, whereas the “no gas” bars show results of corresponding calculations performed using gas-free injection waters.

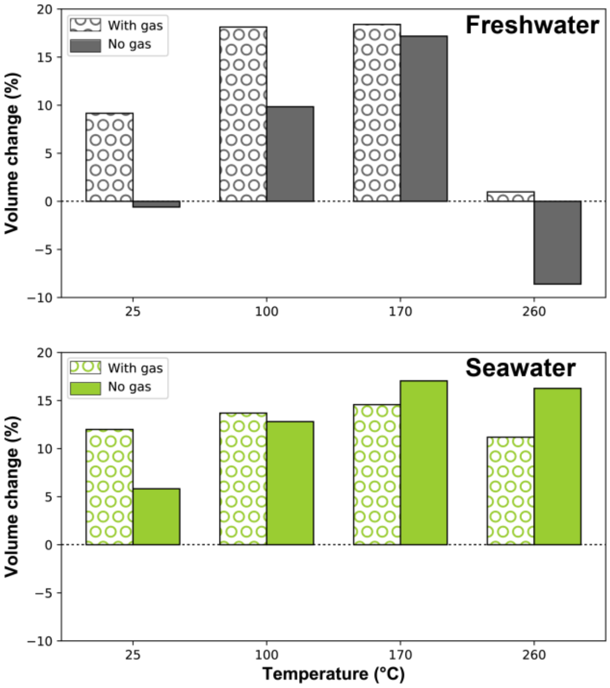

Figure 9. Plots summarizing the differences between freshwater and seawater reaction path model results in the gas-charged systems with lower DIC concentrations as a function of temperature in terms of a) mass of basaltic glass dissolution required to mineralize 90% of the injected DIC; b) rock volume change when 90% of the injected DIC is mineralized; and c) reaction rates of basaltic glass as predicted by the Arrhenius equation (Arrhenius, 1889), with an activation energy of 25.5 kJ/mol (Gislason and Oelkers, 2003) normalized to rates at 25 °C.

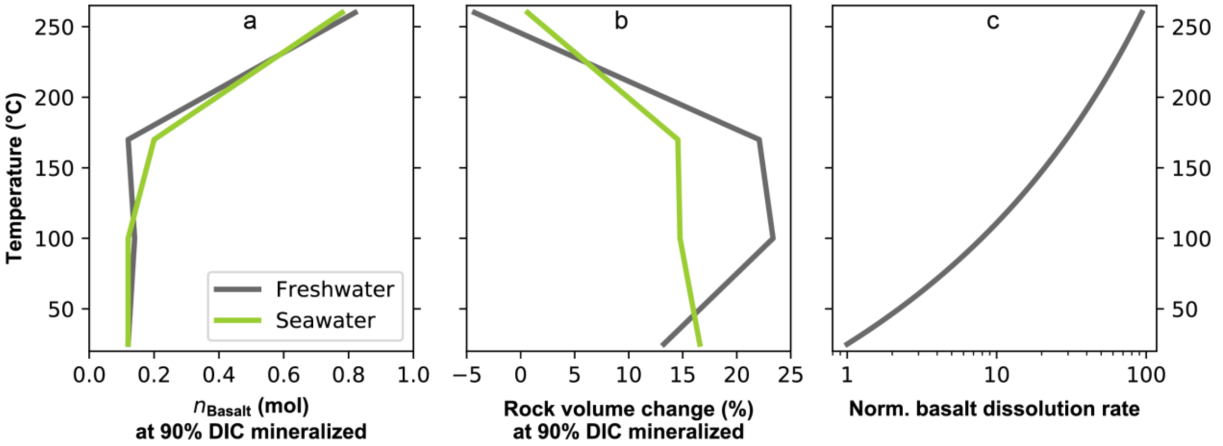

Figure 10. *Extent of* sulfur oxidation-reduction (redox) reactions determined as the concentration difference between sulfide (S^{2-}) precipitated as pyrite and aqueous sulfide from the injected H_2S in seawater, as a function of dissolved basaltic glass. Note the pyrite reaction in the *carbfix.dat* thermodynamic database: $FeS_2 + H_2O = 0.25H^+ + 0.25SO_4^{2-} + Fe^{2+} + 1.75HS^-$. Positive values of ΔS^{2-} indicate sulfate reduction reaction, negative ΔS^{2-} sulfide oxidation reaction, and $\Delta S^{2-}=0$ no detectable redox reactions. The dashed line represents the quantity of dissolved basaltic glass above which the S^{2-} concentrations are <1 mmol/kgw (see text for explanation).